2018

High Resolution Radiation Detectors Based On 4H-SiC N-Type Epitaxial Layers And Pixilated CdZnTe Single Crystal Devices

Cihan Oner
University of South Carolina

HIGH RESOLUTION RADIATION DETECTORS BASED ON 4H-SIC N-TYPE EPITAXIAL LAYERS AND PIXILATED CDZNTE SINGLE CRYSTAL DEVICES

by

Cihan Oner

Bachelor of Science
Mersin University, 2010

Master of Engineering
University of South Carolina, 2014

Submitted in Partial Fulfillment of the Requirements

For the Degree of Doctor of Philosophy in

Electrical Engineering

College of Engineering and Computing

University of South Carolina

2018

Accepted by:

Krishna C. Mandal, Major Professor

Guoan Wang, Committee Member

Xiaofeng Wang, Committee Member

Yuriy V. Pershin, Committee Member

Cheryl L. Addy, Vice Provost and Dean of the Graduate School

DEDICATION

I would like to dedicate this work to my beloved parents and my brother who has always been there for me and showed their support, trust, and love in me throughout my life. I am deeply indebted them all.

ACKNOWLEDGEMENTS

Foremost, I would like to share my eternal gratitude to my advisor, Dr. Krishna C. Mandal for giving me the opportunity to work with him, for providing me a world-class research environment that made it possible to compete the pioneers of the area we work on, for giving me an unlimited amount of support and guidance throughout my studies as well as his priceless insights of science and technology with great enthusiasm. Also, I would like to express my sincere gratitude to my committee members, Dr. Guoan Wang, Dr. Xiaofeng Wang, and Dr. Yuriy Pershin, for taking their precious time to oversee my research and their support of my work.

I would also like to thank the following individuals that contributed and assisted to me throughout my studies.

- Dr. Mohammad A. Mannan, Dr. Khai V. Nguyen, Dr. Rahmi O. Pak, Mr. Towhid A. Chowdhury, Mr. Haseeb Nazir, Mr. Joshua W. Kleppinger, and Mr. Mohsin Sajjad for providing me their valuable support, assistance, friendship, and knowledge during my studies.

- Dr. Ramesh Krishna, Dr. Sandip Das, Dr. Sandeep K. Chaudhuri, and Dr. Peter Muzykov for their invaluable contributions to build and improve our lab facilities.

- The staff and faculty of the Electrical Engineering Department, USC, for their administrative, technical, and scientific assistance and contributions throughout my Ph.D. studies.

- The staff at various departments of USC for their assistance during my studies.
- The Ministry of National Education of the Republic of Turkey for granting me YLSY Ph.D. scholarship which made it possible for me to conduct my Ph.D. studies.

Finally, I would like to thank my family, friends, and all those who have not been mentioned here. Without their support, this work would not have been possible.

ABSTRACT

Silicon Carbide (SiC) is an indirect wide bandgap semiconductor with high thermal conductivity, high breakdown electric field, high carrier saturation drift velocity, and large displacement energy making it a suitable candidate for replacing conventional radiation detectors based on Si, Ge, CdTe, and CdZnTe (CZT). In this dissertation, fabrication and characterization of high-resolution Schottky barrier detectors for alpha particles using 20 μm thick n-type 4H-SiC epitaxial layers are reported. Schottky barriers were obtained by depositing circular nickel contacts of ~10 mm^2 area.

Room temperature current-voltage (I-V) measurements revealed Schottky barrier heights of the order of 1.7 eV, ideality factor of ~1.1, and leakage currents as low as 1 nA at an operating reverse bias of -170 V. Deep level transient spectroscopy (DLTS) revealed the presence of shallow defects at Ec – (0.14 ± 0.01) eV and Ec – (0.18 ± 0.01) eV corresponding to titanium (Ti) substitution in silicon (Si) lattice, and at Ec – (0.62 ± 0.02) eV corresponding to $Z_{1/2}$ defects caused by carbon vacancies. Deep level defects have been found at Ec – (1.42 ± 0.04) eV, and Ec – (1.52 ± 0.03) eV respectively that are related to C-C or C-Si di-vacancies.

A 0.1 μCi ^{241}Am radiation source was used to assess the detector performance by pulse height spectroscopy, and an energy resolution of ~ 0.38% full-width half maxima (FWHM) was observed for alpha particles at ~ 5447 keV. The average diffusion length (L_d) of holes (minority carriers) were calculated to be ~ 13.6 μm using a drift-diffusion

model and MATLAB code. A noise analysis in terms of equivalent noise charge revealed that the white series noise due to the detector capacitance has substantial effect on their spectroscopic performance.

A new edge termination technique was developed by depositing thin Si_3N_4 passivating layer on 4H-SiC epitaxial layer surrounding nickel (Ni) contact in order to improve detector performance. The 4H-SiC detector with Si_3N_4 edge termination showed a higher barrier height with improved rectifying characteristics and a leakage current in pA range, which was two orders of magnitude lower compared to conventional detector fabricated from the same parent wafer. DLTS measurements revealed a reduction in life-time killing defects of detectors with Si_3N_4 edge termination which could be correlated to the observed improvements in energy resolution.

In addition to SiC alpha detector, $Cd_{0.9}Zn_{0.1}Te$ (CZT) based pixelated detectors were fabricated and characterized for gamma ray detection. Large area CZT single crystals has been grown using a tellurium (Te) solvent method. A 3×3 guarded pixilated detector has been fabricated on a ~ 20×20×5 mm^3 crystal cut out from the grown ingot. A guard ring was used to reduce inter-pixel/inter-electrode leakage. I-V measurements revealed a leakage current of ~ 5 nA at a bias voltage of 1000 V and a resistivity of ~ 10^{11} Ω–cm. The mobility-lifetime product ($\mu\tau$) was calculated to be 6×10^{-3} cm^2/V using alpha spectroscopic method. Using time of flight measurements, electron mobility was determined to be ~ 1192 $cm^2.V^{-1}.s^{-1}$. Gamma spectroscopy using a ^{137}Cs source on the pixelated structure showed fully resolved 662 keV gamma peaks for all the pixels, with a resolution (FWHM) of ~ 1.51%, which exhibited a significantly improved resolution.

TABLE OF CONTENTS

LIST OF TABLES

LIST OF FIGURES

LIST OF ABBREVIATIONS

CCE ..... Charge Collection Efficiencies

C-V..... Capacitance-Voltage

CVD .....Chemical Vapor Deposition

CZT .....Cadmium Zinc Telluride

DLTS..... Deep Level Transient Spectroscopy

EMI .....Electromagnetic Interference

ENC..... Equivalent Noise Charge

FWHM .....Full-Width at Half-Maximum

I-V ..... Current-Voltage

keV .....Kilo Electron Volt

MCA ..... Multi-Channel Analyzer

MeV .....Mega Electron Volt

PECVD ..... Plasma Enhanced Chemical Vapor Deposition

PHS ..... Pulse-Height Spectroscopy

PVT ..... Physical Vapor Transport

RIE .....Reactive Ion Etch

RT ..... Room Temperature

RTA.....Rapid Thermal Annealing

SEM ..... Scanning Electron Microscopy

SiC.....Silicon Carbide

SIMS ..... Secondary Ion Mass Spectrometry

Si_3N_4.....Silicon Nitride

SRIM..... Stopping and Range of Ions in Matter

LIST OF SYMBOLS

ϕ_B	Schottky barrier height
ϕ_m	Metal work function
ϕ_n	Semiconductor (n-type) work function
χ	Semiconductor electron affinity
V_{bi}	Built-in potential of metal-semiconductor junction
W	Width of depletion region
n	diode ideality factor
ρ	*R*esistivity
μ	Mobility of the majority carrier
L_d	Minority carrier diffusion length
k_B	Boltzmann constant (8.62×10^{-5} eV/K)
T	Absolute temperature
e	Electron charge (1.6×10^{-19} C)
N_C	Effective density of states in conduction band
N_D	Effective doping concentration
N_t	Trap concentration
ε	Dielectric constant of the semiconductor; which is ~9.72 for 4H-SiC
ε_0	Permittivity of vacuum
A^*	Richardson's constant taken to be 146 $A \cdot cm^{-2}K^{-2}$ for 4H-SiC

I_s	Reverse saturation current
σ_n	Carrier capture cross section
$\langle V_{th} \rangle$	Mean thermal velocity
g	Degeneracy of the trap level and was considered to be equal to 1
ΔE	Energy separation between the trap level and the carrier band
τ	Pulse shaping time
a_f	Coefficient of the FET 1/f noise
b_f	Dielectric noise coefficient

CHAPTER 1

GENERAL INTRODUCTION

1.1 SiC Alpha Particle Detector

Wide bandgap semiconductors are suitable for high temperature, high power, and high frequency applications because of their superior physical, electrical, and opto-electronic properties. Among different wide bandgap materials, silicon carbide (SiC) is one of the most promising semiconductor due to its high radiation hardness, high breakdown electric field, high saturation electron drift velocity, high thermal conductivity, and smaller anisotropy [1] - [10]. 4H-SiC based nuclear radiation detectors have the most appealing characteristics for harsh environment applications where conventional semiconductors (e.g., Si, Ge, CdTe, CdZnTe) showed inadequate performance [11] - [16]. Amongst all of the SiC polytypes, 4H-SiC has the most compatible properties due to its large displacement energy (Ed_{Si} = 3.5 eV and Ed_C = 22 eV), high bulk electron mobility (1000 $cm^2/V.s$), high thermal stability (2857 ^oC sublimation point), smaller anisotropy, and, more importantly, its wide bandgap (3.27 eV at 300 K). [17] - [24].

Although SiC possesses superior properties, the conventional growth techniques result in crystal defects in the microscopic levels limiting the nuclear detection performance [25] - [28]. Major defects present in SiC are edge dislocations, screw dislocations, carrot defects, comet defects, triangular defects, and basal plane dislocations

[6], [22], [29]. Most of these defects are normally confined to the substrate [30] but some screw dislocations can propagate to the epitaxial layer and form micropipe defects in the epilayer [31].

Babcock et al. were the first to demonstrate alpha particle detectors based on SiC Schottky diodes [32] and Nava et al. were the first to report 5.48 MeV alpha particle signal in 4H-SiC epitaxial detectors [33]. Ruddy et al. demonstrated an energy resolution of 5.8% and 6.6% for deposited energy of 294 keV and 260 keV, respectively, by alpha particles from a collimated ^{238}Pu source [34]. In 2009 Ruddy et al. reported an energy resolution of 5.7% for a deposited energy of 89.5 keV alpha particles from a collimated ^{148}Gd source with 10 μm thick epilayer detector [35]. In another article, Ruddy et al. [36] reported fabrication of high-resolution alpha particle detectors with aluminum guard ring structures using which they obtained an energy resolution close to 46 keV for alpha particles from a ^{238}Pu source. These SiC epitaxial layers still suffered from electrically active defects [37] - [42], prohibited them to achieve an energy resolution comparable to high-purity germanium (HP Ge) or lithium-drifted silicon Si (Li) detectors [43].

In the last decade, substantial progress has been made in advanced vapor-phase epitaxy for growing SiC epitaxial layers. Availability of high resistive and high-quality detector grade SiC epitaxial layers with extremely low micropipe concentrations created renewed interest in SiC based radiation detectors [6], [42], [44] – [46]. The reported results show that SiC detectors are uniquely suited for alpha-particles, neutrons, and gamma-ray monitoring applications in room- or elevated-temperature environments even where high-intensity gamma-rays are present. Recent results [44] have shown that SiC detectors operate well in temperatures up to 700°C.

With the expansion of nuclear power and development of advanced nuclear fuel cycle processes, there is a growing need for high performance, solid-state nuclear detectors capable of operating for extended times at elevated-temperatures (300°C – 600°C) and high radiation fluxes. Silicon carbide (SiC) radiation detectors are excellent candidates for such environments, since the material is extremely radiation hard and chemically inert. In nuclear fuel safeguards application, the potential diversion of nuclear materials can require continuous, long-term monitoring. SiC detectors are well suited for this application. SiC detectors have been demonstrated also to withstand high gamma-ray doses that exceeded anticipated doses for any long-term monitoring applications [47]. SiC detectors can be deployed in key locations on spent fuel assemblies at either commercial fuel storage locations or government fuel storage repositories. The detectors could be installed at any time following discharge and could potentially monitor both the neutron and gamma-ray activity from discharge, during transportation and long-term storage. Diversion of fuel assemblies or changes to the neutron and gamma-ray output due to tampering or physical changes to assemblies from physical or chemical degradation can be detected through unexpected changes in the observed neutron and gamma-ray activities. Other applications of SiC nuclear detector will include monitoring of space nuclear reactors, neutron dose monitoring of reinforced concrete structures, detecting and quantifying special nuclear materials (SNMs) for safeguards, national security, and verification for nuclear treaty enforcement.

1.2 CZT Gamma-Radiation Detector

Currently the most widely used detectors for gamma radiation are based on high-purity germanium (Ge). Ge has high atomic number for gamma-ray stopping and offer

excellent energy resolution (0.2% at 662 keV) [48]. However, Ge detectors must be cooled to cryogenic temperatures to obtain such high-energy resolution due to the relatively small bandgap energy (0.7 eV at 300K) [49]. The small bandgap leads to excessive dark current at room temperature, which can be reduced to an acceptable level upon cryogenic cooling. However, cooling makes the detection system bulky and increases power consumption. Wide bandgap compound semiconductors are therefore more suitable for gamma detector at room temperature operation.

One of the most promising semiconductor materials used in gamma detectors is single crystal cadmium zinc telluride or CZT ($Cd_{0.9}Zn_{0.1}Te$). CZT is a direct-bandgap semiconductor grown by alloying CdTe and Zn using Bridgman growth technique [50]. CZT has a bandgap energy of 1.58 eV at 300K and resistivity of 10^{11} Ω.cm resulting in low dark current at room temperature [51]. Due to high average atomic number (Z = 50), CZT offers quite good x-ray and gamma-ray stopping power. Properties like adequate gamma-ray energy absorption even for small volume detectors, low leakage current, high density and ease of detector fabrication has made it a very suitable candidate for nuclear radiation detection [51] – [54].

With growing concerns about nuclear proliferation and terrorism, there are needs for portable, high performance nuclear spectrometers. CZT radiation detector could play an important role in this matter and could be used for screening of radioactive materials at the port of entry, for detection of dirty bomb or special nuclear materials to combat security threat, for detection of illicit radioactive enrichment during non-proliferation treaty verification, for monitoring and safeguard of nuclear spent fuel. X-ray and gamma-ray detectors based on CZT material could also be used in industrial process monitoring,

nondestructive testing, medical imaging such as positron emission tomography (PET), and high energy astrophysics & astronomy.

CZT crystals suffer from poor growth yield due to defects and inhomogeneity, making the detector material very costly [55]. Macroscopic defects in CZT materials such as cracks and twin/grain boundaries and microstructural defects such as mosaic structures, tilt boundaries, dislocations, impurities, tellurium inclusions/precipitations lead to poor charge transport properties [56]. Performance of large volume CZT detectors is further limited by poor charge transport properties like low drift-mobility and lifetime especially for holes. CZT has much higher electron mobility compared to hole mobility (μ_e = 1000 $cm^2/V.s$ and μ_h = 50 $cm^2/V.s$), so a polarization effect is observed even at a high bias voltage [57]. To compensate for poor hole transport properties, specialized detector geometries such as coplanar, multipixel, and Frisch grid detector structures where readout signal is due to electron movement only are adapted [58]. In this dissertation, multipixel CZT detector structure in a unipolar charge sensing mode has been investigated. In this approach, the induced pulse is mostly due to electron motion in the detector and the hole contribution to the signal is negligible, thereby reducing the effect of hole trapping.

1.3 DISSERTATION OVERVIEW

Primary focus of this dissertation was fabrication and characterization of Ni/4H-SiC epilayer Schottky barrier detectors on 20 μm thick n-type SiC epitaxial layer. New edge termination using passivating Si_3N_4 layers was developed in order to reduce surface leakage current and to improve energy resolution. Electrical characterization of the fabricated detectors was carried out using current-voltage (I-V) and capacitance-voltage (C-V) measurements to evaluate Schottky barrier junction properties. Defect analysis using

capacitance-mode deep level transient spectroscopy (DLTS) was performed to identify deep and shallow defect levels that may be detrimental to detector performance. Electronic noise analysis of front-end readout system was developed in terms of equivalent noise charge (ENC) using MATLAB program. Charge collection efficiency and detector performance was evaluated using pulse-height spectroscopy (PHS) measurements with an ^{241}Am radiation source (5.48 MeV).

These investigations and results are described in the following chapters of this dissertation. Chapter 2 provides a summary of 4H-SiC properties that are relevant to high-performance radiation detector and motivated to choose this semiconductor as the detector material of interest. Chapter 2 also briefly reviews the growth of 4H-SiC material followed by 4H-SiC detector fabrication on 20 μm thick n-type SiC epitaxial layer.

Chapter 3 includes electrical characterization and defect analysis of Ni/n-type 4H-SiC detectors on 20 μm epilayer. This chapter provides a theoretical background on Schottky barrier contacts, reviews thermionic emission model used for detector characterization, and discusses the results of current-voltage (I-V) and capacitance-voltage (C-V) measurements. Finally, results and analysis of defects in fabricated n-type 4H-SiC detectors using deep level transient spectroscopy (DLTS) are reported.

Chapter 4 describes the systematic study of 4H-SiC detector performance as an alpha particle detector using pulse-height spectroscopy (PHS). Radiation detection performance in terms of charge collection efficiencies (CCE) as a function of bias voltage for 5.48 MeV alpha particles are also reported in this chapter. Using a drift-diffusion model, minority carrier diffusion length and contribution of hole diffusion to the charge collection efficiency are explained.

Chapter 5 reports results of 4H-SiC Schottky barrier detectors with passivating silicon nitride (Si_3N_4) edge termination layers with the goal of reducing surface leakage current in order to improve energy resolution. The junction properties, defect levels, and energy resolution with alpha spectroscopy are evaluated for the edge-terminated detectors, and experimental results are compared to baseline detector without edge termination to assess edge termination effectiveness.

In addition to 4H-SiC radiation detectors, multipixel CZT detector structure have also been investigated during this dissertation study. In this approach, the unipolar signal induction is achieved in a pixelated detector array by keeping the pixel size small as compared to the detector thickness. The multipixel CZT detectors were characterized with low leakage current under operating conditions. Electron drift mobility and $\mu\tau$ product have been measured using alpha-ray spectroscopy and a time of flight technique respectively. Gamma ray spectroscopic measurements were performed by using ^{137}Cs radiation source of 662 keV. A MATLAB based correction scheme was developed to improve digitally obtained pulse-height spectra. Results of multipixel CZT detectors have been reported in Chapter 6.

Finally, Chapter 7 concludes the research presented in this dissertation and provides suggestions for future work.

CHAPTER 2

DETECTOR FABRICATION ON SILICON CARBIDE EPITAXIAL LAYER

2.1 FAVORABLE PROPERTIES OF 4H-SIC FOR RADIATION DETECTION

Depending on staking sequences of silicon and carbon bilayers, silicon carbide (SiC) exhibits different crystal lattice structures called polytypes, which can have significantly different optical and electrical properties such as band-gap, drift velocity, breakdown electric field strength, and the impurity ionization energies [59] - [62]. Among different polytypes, 4H-SiC, which has hexagonal symmetry with four-bilayer stacking periodicity, offers appealing characteristics such as a wide bandgap, high bulk electron mobility, large displacement energy, high thermal stability, and smaller anisotropy [12], [17], [18], [24], [63] – [66]. Table 2.1 summarizes the properties of 4H-SiC that are relevant for radiation detector fabrication. With a wide bandgap energy of 3.27 eV and resistivity $>10^{10}$ Ω-cm at 300 K, 4H-SiC offers very low leakage currents (a few nA or lower) at operating bias resulting in very low thermal noise. Lower dielectric constant of 4H-SiC (9.7 compared to 11.9 for Si and 16.0 for Ge) helps to reduce the detector capacitance for a given active detector volume allowing greater charge collection efficiency and decreased white series noise component. Good charge transport properties such as high bulk electron mobility (1000 cm^2/V-s) and saturation electron drift velocity (2 x 10^7 cm/s) increases

charge collection probability and thereby signal resolution. High thermal stability (2857 ^{o}C sublimation point) and better thermal conductivity (280 W/mK) of 4H-SiC allows for detector operation well above room temperature. High displacement energies of the constituent elements (Ed_{Si} = 35 eV and Ed_{C} = 22eV) of 4H-SiC indicates high radiation hardness of the material and make it suitable for detectors deployed in harsh environments. For these superior electronic properties and physical ruggedness, 4H–SiC has been identified as promising semiconductor for nuclear radiation detector operable at room or elevated temperature.

Table 2.1 Properties of 4H-SiC

Property	**4H-SiC**	**Expected Radiation Performance**
Band gap (eV) at 300K	3.27	Offers low leakage current resulting in low thermal noise, consequently better signal to noise ratio
Resistivity (Ω-cm) at 300K	$>10^{10}$	
Electron hole pair creation energy (eV)	7.28	Increased charge generation resulting in increased signal and energy resolution
Lower dielectric constant	9.7	Contributes toward higher charge conversion efficiency and storage
High breakdown field (MV/cm^2)	3.0	Possibility of achieving high signal to noise ratio
Electron mobility (cm^2/V-s)	1000	Offers good charge transport properties contributing to high charge collection efficiency
Saturation electron drift velocity ($x10^7$ cm/s)	2	
Thermal conductivity (W/mK)	280	Possibility for high temperature operation
High melting point (˚C)	2830	
Threshold displacement energy (eV)	Ed_{Si} = 35 Ed_{C} = 22	Capability of operation under high radiation background

2.2 Growth of Epitaxial 4H-Silicon Carbide Detector Material

Conventional growth of SiC bulk crystal is performed using physical vapor transport (PVT) technique [67]. Bulk SiC crystals grown by this method, often suffer from microscopic crystallographic defects such us dislocations, micropipes, carrot defects, and non-uniformity. These intrinsic defects in semiconductor act as carrier traps or recombination centers leading to poor charge collection efficiency and poor detector performance [25] – [28]. Over the years, efforts have been made to better control thermal gradients inside the growth chamber in order to defect density in SiC bulk crystal [68], [69]. Nevertheless, commercially available bulk SiC still has relatively high defect densities to be used for high performance detector devices. Development of SiC epitaxial layers on bulk SiC substrate using techniques such as chemical vapor deposition (CVD) has demonstrated the feasibility of high-performance nuclear radiation detectors as epitaxial growth yields much higher quality SiC material [70]. SiC epilayers offer high crystallinity, higher growth controllability and reproducibility compared to its bulk counterpart.

For present studies, 20 μm thick 4H-SiC epitaxial layers were grown on 76 mm diameter wafers diced from highly nitrogen-doped 4H-SiC (0001) substrates with a 4^{o} offcut towards the $[11\bar{2}0]$ direction. The epitaxial layer forms the detector 'active layer' is grown by hot-wall CVD system using dichlorosilane (SiH_2Cl_2, DCS) and propane (C_3H_8) precursor gases with hydrogen (~ 6 SLM) as the carrier gas. A dilution ratio of ~ 1000 was used and flow rates of precursors were maintained to obtain a C/Si ratio of ~ 1.28. The growth temperature and pressure were kept at 1550°C and 80 - 120 torr, respectively.

Secondary ion mass spectrometry (SIMS) measurement was performed to characterize the epilayer layer thickness and doping profiles. Wafers were evaluated by Nomarski optical microscopy and scanning electron microscopy (SEM), and micropipe defect density was found to be < 1 cm^{-2}.

2.3 EPITAXIAL LAYER THICKNESS

The 4H-SiC detectors are intended for monitoring and accounting of alpha particles. The incident alpha particles interact with the electrons in valence band of absorbing semiconductor atoms (SiC epitaxial layer). When the magnitude of this interaction is large enough to excite the electrons to a higher energy band removing them from the atoms, electron-hole pairs are created that leads to a loss of energy in alpha particles. These radiations generated charge carriers are separated under applied electric field, and are then collected by respective electrodes generating a current signal. When a charge particle of mass m with kinetic energy E interacts with an electron of mass m_0, the maximum transferable energy is $4Em_0/m$ in a single collision. Using SRIM 2012 software [71], the electronic stopping power of the alpha particles in 4H-SiC (dE/dx where x is penetration depth) was calculated to be ~ 18 μm in SiC for 5.486 keV alpha particle. Figure 2.1 represents a Bragg curve that shows the energy loss of 5.48 MeV alpha particle as a function of depth of penetration during interaction with 4H-SiC detector materials. It can be seen from the curve that the penetration depth of alpha particle in 4H-SiC epitaxial layer is ~ 18 μm. Maximum loss of energy for the alpha particles occurs at the end of the range, which is typical of charged particle interaction with matter [48]. As per these results, the thickness of the epitaxial layer, which is the detector region of the device, should be 18 μm or larger to capture all of the energy of incident alpha particle to obtain a high signal to

noise ratio. Hence, in this dissertation, we have studied 20 μm thick epitaxial layer of 4H-SiC detectors.

Furthermore, resolution of a radiation detector is a function of collection efficiency of charge carriers generated by alpha particles. Charge carriers produced in the depletion region and in neutral region both could contribute to detector signal. However, probability of collection is much higher for charges generated within the depletion region (space charge region) compared to charges generated in the neutral region. Thus a sufficiently large depletion width, which defines the active volume within the detector, is also another crucial requirement for obtaining high energy-resolution and high efficiency detection. Chapter 4 address this issue.

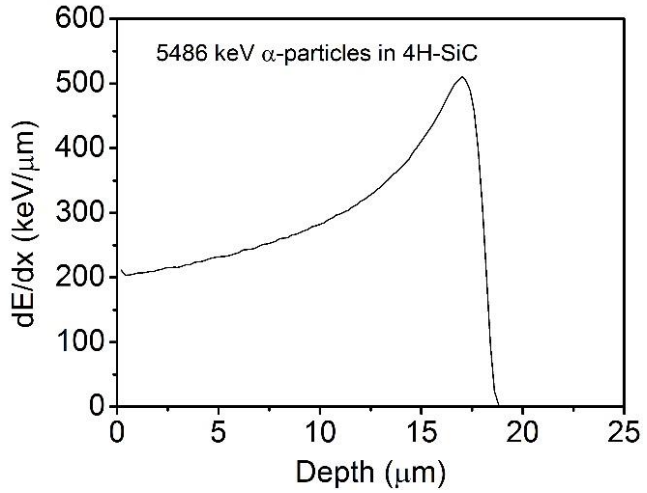

Figure 2.1. Energy loss of 5.48 MeV alpha particle as a function of penetration depth.

2.4 Ni/4H-SiC Schottky Barrier Detector Fabrication

Planar, single-pixel detector was fabricated on 20 μm n-type 4H-SiC epitaxial layers, where metal contacts are placed on both sides of the detector material. The detector material consists of 20 μm thick active layer that is 4H-SiC epitaxial layer, a very thin

(1μm) 4H-SiC buffer epilayer, and finally 4H-SiC bulk substrate layer. A circular nickel (Ni) Schottky barrier contact on the epilayer face forms top contact. This acts as the 'detector window' through which ionizing radiation is captured. A large square contact deposited on the bulk SiC side form the bottom contact. The cross-sectional schematic of 4H-SiC epitaxial detector is presented in Figure 2.2

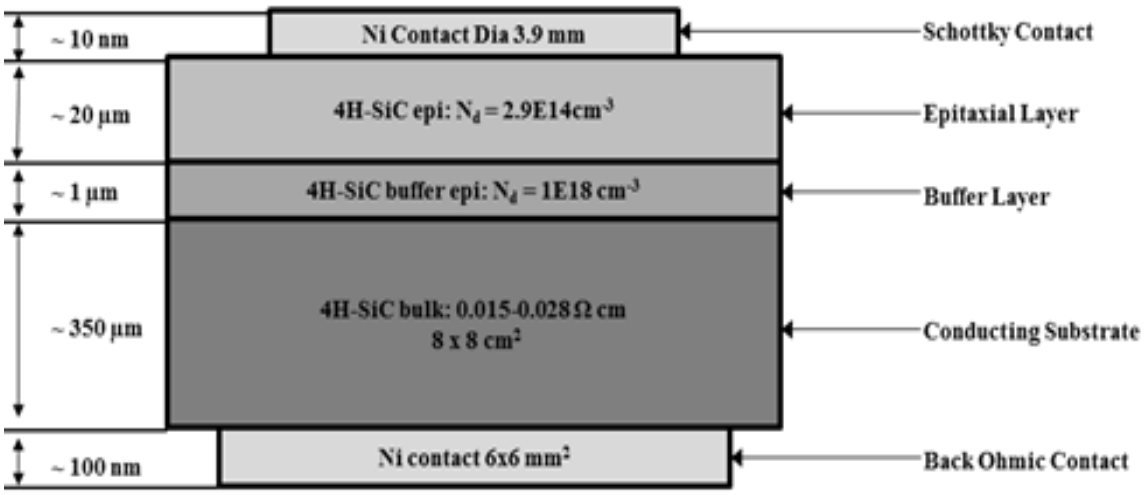

Figure 2.2 Cross-sectional view of Schottky barrier detector fabricated on n-type 20 μm thick 4H-SiC epitaxial layer.

Following a modified RCA cleaning of SiC wafer, first a square ~ 6 × 6 mm^2 and 100 nm thick Ni bottom contact is deposited on the bulk SiC (C-face) using a Quorum Q150T DC sputtering unit and a shadow mask, followed by rapid thermal annealing (RTA) at 950°C for 2 minutes in high-purity argon (Ar). Next a 3.9 mm diameter and ~ 10 nm thick circular window for Schottky contact was deposited on top of the epitaxial layers (Si-face) using photolithography technique. A Karl Suss MA-6 mask aligner was used in conjunction with a predesigned quartz photo-mask containing a 3.9 mm circular patch used

for centering of the metal contact and exposure of the photoresist coated samples. After exposing and developing of the photoresist, a 10 nm Ni was deposited by DC sputtering employing a Quorum 150T sputtering unit followed by liftoff process where a 3.9 mm Ni Schottky contact remained. After fabrication, the detector was mounted on a printed circuit board (PCB) designed and fabricated in our laboratories and wire bonded using very thin (25 μm) gold wire. A photograph (top view) of a fabricated detector is shown in Figure 2.3.

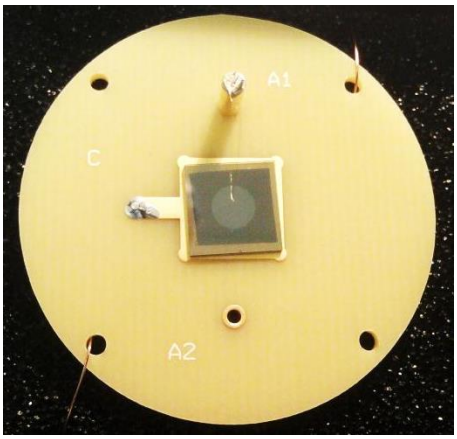

Figure 2.3 Photograph of a 4H-SiC epitaxial Schottky barrier detector with circular nickel top contact mounted on a PCB.

2.5 Fabrication of 4H-SiC Detector with Edge Termination

In preparation for Si_3N_4 thin passivating film for edge termination, the top and bottom Ni contacts of 4H-SiC detectors were etched away using dilute nitric acid followed by a modified RCA cleaning procedure. A Si_3N_4 layer with approximate thickness of 400 nm was deposited on the epilayer surface using a STS Plasma Enhanced Chemical Vapor Deposition (PECVD) system. The deposition chamber was seasoned by running the process for five minutes prior to the actual run. The deposition parameters used were the following: temp process 300 ˚C, temp aux 250 ˚C, pressure 800 mtorr, power (13.56 MHz

RF) 25 W. Gases and flow rates were 2% silane balance nitrogen at 2000 sccm and ammonia at 40 sccm. The Si_3N_4 layer thickness was determined to be approximately 410 nm using a Nanospec Reflectometer. As previously mentioned photolithography process was repeated prior to the use of a Vision Reactive Ion Etch (RIE) system to open a window in the Si_3N_4 layer with a slight over-etch to ensure epilayer was completely exposed for Schottky contact formation. A 10 nm thick Ni contact was once again deposited using the process mentioned previously. A cross-sectional view of the detector following edge termination with Si_3N_4 is shown in Figure 2.4.

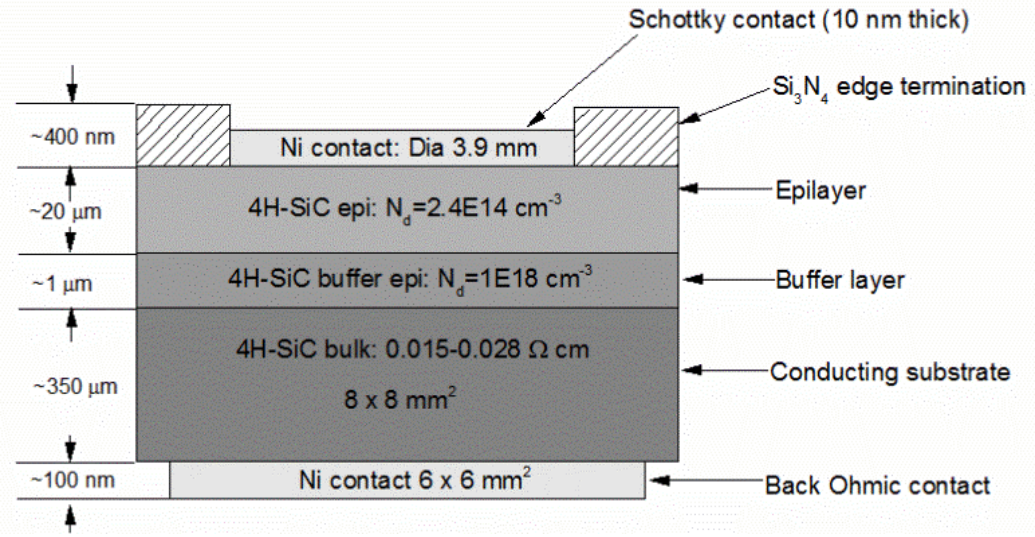

Figure 2.4 Cross-sectional view of the edge terminated Schottky barrier radiation detector. Si_3N_4 layer surrounds the Ni contact.

CHAPTER 3

CHARACTERIZATION OF 4H-SIC RADIATION DETECTOR ON EPITAXIAL LAYER

3.1 OVERVIEW

Schottky-diode radiation detectors were fabricated on n-type (nitrogen-doped), 20 μm thick 4H-SiC epitaxial layer using nickel contacts as described earlier. Fabricated detectors were characterized using current-voltage (I-V) and capacitance-voltage (C-V) measurements. A thermionic emission model [72] was used to determine important Schottky barrier junction properties such as leakage current, doping concentration, built-in potential, Schottky barrier height, and diode ideality factor, which are predictive of device quality and performance. Deep level transient spectroscopy (DLTS) measurements were carried out to investigate defect levels in the detector active volume, which may act as generation-recombination centers and can lead to increased detector leakage current.

3.2 SCHOTTKY BARRIER DETECTOR STRUCTURE

Planar, single-pixel detectors are fabricated on 20 μm n-type 4H-SiC epitaxial layers, where metal contacts are placed on both sides of the detector material. Of this detector structure, most important part is the formation of Schottky barrier junction between Ni metal and 4H-SiC epilayer as it forms the ‘detector window’ through which ionizing radiations are captured by the 4H-SiC epilayer. Therefore, characterization of the

Schottky barrier junction is of great importance to predict detector performance. Figure 3.1 shows energy band diagram of an ideal Schottky barrier junction between a metal and an n-type semiconductor at thermal equilibrium.

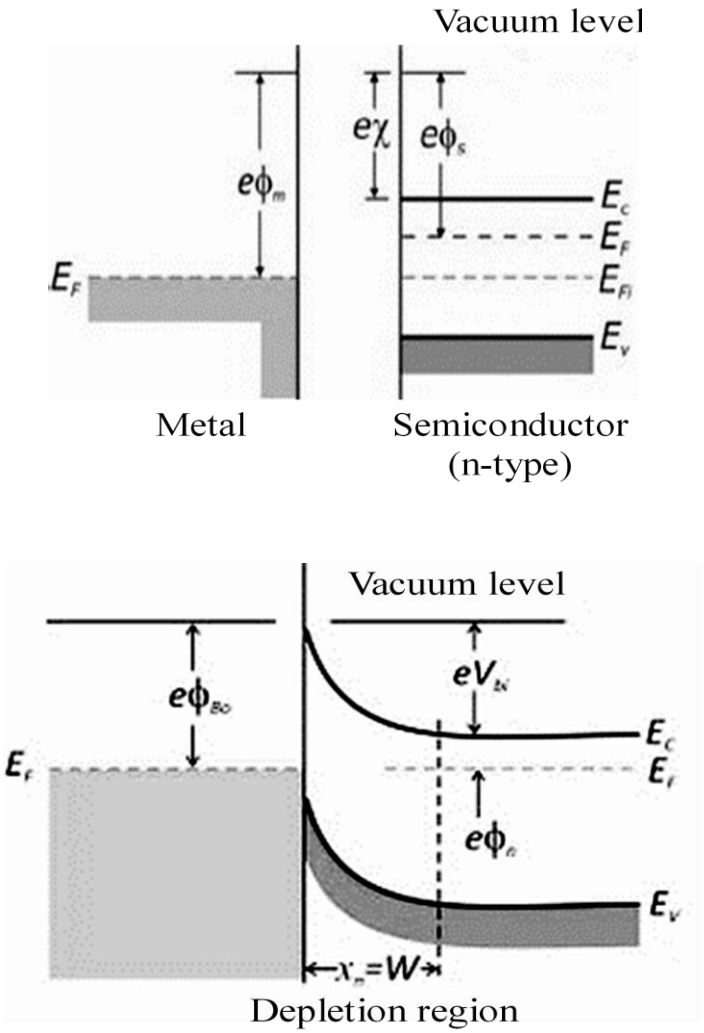

Figure 3.1 Energy band diagram of metal and n-type semiconductor before contact (top) and Schottky barrier junction between metal and n-type semiconductor after contact formation (bottom) at thermal equilibrium [73].

A metal-semiconductor junction is called Schottky barrier junction when at the interface of the junction a barrier to charge transport is formed due to the difference between metal work function ($e\phi_m$) and semiconductor electron affinity ($e\chi$). The barrier height ($e\phi_{B0}$) restricts electron injection from the metal into the semiconductor providing

a rectifying effect so that current conduction occurs only at forward bias. Ideally at reverse bias, there should not be any conduction, however in reality a low saturation current (leakage current) is present. To form Schottky contact with an n-type semiconductor, metal work function ($e\phi_m$) must be higher than n-type semiconductor work function ($e\phi_n$) and the Schottky barrier height could be determined using following equation.

$$e\phi_{B0} = e\phi_m - e\chi \quad (3.1)$$

On the semiconductor side, the barrier for electron flow from semiconductor conduction band into the metal is known as the built-in potential (V_{bi}) and is given by:

$$e\phi V_{bi} = e\phi_{B0} - e\phi_n \quad (3.2)$$

The Schottky barrier height ($e\phi_{B0}$) of a metal-semiconductor junction should remain constant with respect to the polarity of the applied voltage, but built-in potential (eV_{bi}) decreases or increases with applied forward or reverse voltage, respectively. In 'forward' bias, where a positive voltage is applied to the metal in respect to the semiconductor, V_{bi} is reduced so electrons can flow more easily from semiconductor into metal. The built-in voltage (V_{bi}) in an n-type semiconductor is given by:

$$V_{bi} = \phi_B - \frac{k_B T}{e} ln\left(\frac{N_C}{N_D}\right) \quad (3.3)$$

where ϕ_B = Schottky barrier height,

k_B = Boltzmann constant (8.62×10^{-5} eV/K),

T = absolute temperature,

e = electron charge (1.6×10^{-19} C),

N_C = effective density of states in conduction band, and

N_D = effective doping concentration

During contact formation, due to conduction band bending, free electrons in n-type semiconductor at the vicinity of the contact interface are removed exposing positive charge and creating a depletion region, which is extended only to semiconductor side. In the metal side a neutralizing negative charge is accumulated at the contact interface. Thus an electric field develops at the metal-semiconductor interface. At the edge of the depletion region, the electric field falls to zero and the energy bands become flat to match with the bulk region value as shown in Figure 3.1. The width of the depletion region for a Schottky barrier is mostly negligible at forward bias, but increases with applied reverse bias. An applied reverse bias to the metal-semiconductor Schottky barrier junction increases the potential difference across the junction, which increases the net charge density and thereby extending the width of the depletion region, where radiation-induced charge carriers are collected. If applied reverse bias voltage is large enough that the depletion width is extended throughout the detector active region (epitaxial layer thickness), a 'fully depleted' detector is created. The width of the depletion region, *W,* in n-type semiconductor is expressed as:

$$W = \sqrt{\frac{2 \times V_{bi} \times \varepsilon \times \varepsilon_0}{e \times N_D}} \qquad 3.4$$

where ε = dielectric constant of the semiconductor; which is ~9.72 for 4H-SiC,

ε_0 = permittivity of vacuum,

e = electronic charge (1.6×10^{-19} C),

N_D = effective doping concentration and

V_{bi} = built-in potential

Using the expression for resistivity (ρ) = $1/eN\mu$, where μ is the mobility of the majority carrier (electrons for n-type SiC), the Equation 3.4 can be written as:

$$W = \sqrt{2V_{bi}\varepsilon\varepsilon_0\mu\rho} \qquad 3.5$$

The radiation-induced charge carriers are collected most efficiently if generated in the depletion region. Therefore, practical detector requires high enough reverse applied bias to obtain largest depletion region possible, without large reverse saturation current. Also from Equation 3.5, it is imperative that the semiconductor should have high resistivity as possible in order to obtain a large depletion width. The resistivity is limited by the purity of the semiconductor material, thus it is highly important to fabricated detectors on defect-free and highly pure material.

As positive charge accumulates in the n-type semiconductor side and negative charge at the metal side of the junction, the depletion region behaves like charged capacitor. The junction capacitance per unit area at an applied reverse bias of *V* is expressed as:

$$C = \left(\frac{\varepsilon\varepsilon_0 eN_D}{2(V_{bi} - V)}\right)^{1/2} \qquad 3.6$$

When reverse bias is applied, depletion region (space charge region) grows wider and the capacitance per unit area decreases. At high reverse bias when a detector becomes fully or highly depleted, the maximum electric field will occur and the junction capacitance will become very small. This condition is ideal for charge carrier movements due to drift velocity increasing charge collection efficacy significantly and thereby detector resolution.

3.3 CURRENT-VOLTAGE MEASUREMENTS

Using a Keithley 237 High Voltage SMU, current-voltage (I-V) measurements were carried out for planar Schottky detector fabricated on 20 μm epitaxial layer 4H-SiC. The forward-biased I-V characterizations were used to study the properties of the Schottky contacts such as barrier height and the diode ideality factor. The reverse I-V characteristics were used to determine the leakage current under operating conditions. An electronic box made up of aluminum was used during the measurements to shield the detector against any electromagnetic interference (EMI). Figure 3.2 shows a typical I-V characteristic at room temperature for an n-type 4H-SiC epitaxial (20 μm) Schottky detector with Ni-contact. The variation of observed current as a function of applied bias voltage across the detector clearly shows rectifying Schottky behavior of the device

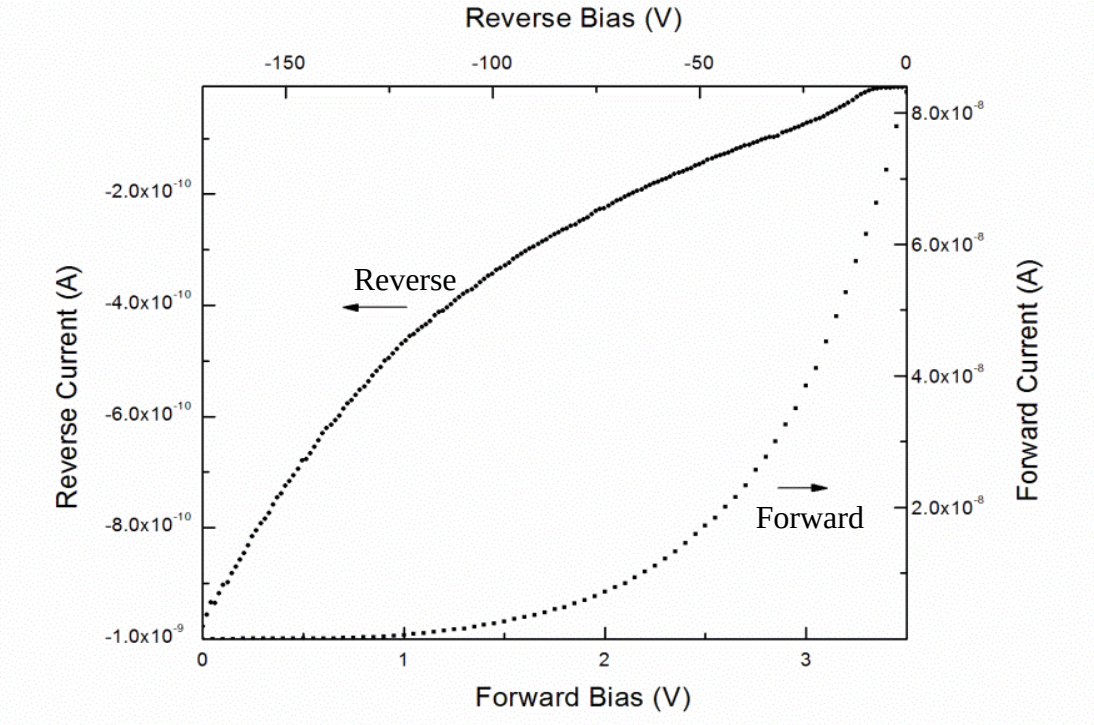

Figure 3.2 Current-Voltage characteristics of an n-type 20 μm 4H-SiC epitaxial/Ni Schottky detector at room temperature.

Thermionic emission model, which is for thermally induced flow of charge carriers over a potential barrier [74], was applied to the forward bias region of the I-V characteristics. As per this model, the measured current *I* in a Schottky barrier junction for the applied bias *V* can be given by:

$$I = A^* A T^2 \left(exp^{-\frac{e}{k_B T}\phi_B} \right) \left(\exp^{\left(\frac{eV}{nk_B T}\right)} - 1 \right) \quad 3.7$$

where A^* = Richardson's constant taken to be 146 A·cm^{-2}K^{-2} for 4H-SiC [8], [10],

A = diode area,

T = absolute temperature,

e = electron charge (1.6 × 10^{-19} C),

k_B = Boltzmann constant (8.62 × 10^{-5} eV/K),

ϕ_B = Schottky barrier height, and

n = diode ideality factor.

Using logarithm expression, the Equation 3.7 could be written as a linear equation as given below where I_s is the saturation current, $I_s = A^* A T^2 \left(exp^{-\beta \phi_B} \right)$ and $\beta = q/k_B T$:

$$log(I) = \frac{\beta V}{n} + log(I_s) \quad 3.8$$

The saturation current I_s then can be obtained from the intercept and the ideality factor 'n' could be measured from the slope using following equation:

$$n = \frac{1}{slope \times {}^{1}/_{\beta}} . \quad 3.9$$

Schottky barrier height (Φ_B) can be determined using following expression:

$$\Phi_B = \frac{k_B T}{q} \ln\left(\frac{A A^* T^2}{I_0} \right) \quad 3.10$$

Applying the thermionic emission model as discussed in Equation 3.7, a Schottky barrier height (Φ_B) of the fabricated diode was calculated to be 1.13 eV using Equation 3.10. A linear fit was applied to the forward current region of the semi logarithmic I-V plot to determine the diode ideality factor using Equation 3.9 and was determined as 1.19. Barrier height specifies the amount of current flow through the junction and the ideality factor specifies the spatial uniformity of the barrier height across the diode surface [75]. The ideality factor greater than 1 suggests presence of charge traps resulting from recombination of the charge carriers and inhomogeneity in the depletion region [12], [76] - [78]. Up to -170 V bias was applied during the I-V measurements, and at this bias voltage, the dark current (reverse bias leakage current) was measured to be ~1 nA at room temperature. Leakage current at applied reverse bias across the detector is also an important property as the detector electronic noise increases with leakage current thereby reducing the overall detector resolution [79].

3.4 Capacitance-Voltage Measurements

Capacitance-voltage (C-V) measurement at a frequency of 1 MHz was carried out at room temperature under dark condition. The C-V measurement provided values of effective carrier concentration (N_D) in n-type 4H-SiC epitaxial layer and built-in potential (V_{bi}) of Schottky detector. The junction capacitance of Schottky barrier at an applied reverse bias depends on the depletion region width and is expressed as shown in Equation 3.6, which can be rearranged as following where A is detector area:

$$\frac{1}{C^2} = \frac{2V_{bi}}{e\varepsilon A^2 N_D} + \frac{2V}{e\varepsilon A^2 N_D} \qquad 3.11$$

Applying a linear fit where $1/C^2$ is plotted against applied voltage bias, V, built-in voltage (V_{bi}) could be estimated, from the intercept, and the effective doping concentration (N_D) could be determined from the slope using the following formula:

$$N_D = \frac{2}{e\varepsilon A^2 \times slope} \qquad 3.12$$

Once doping concentration and built-in voltage is determined, the barrier-height (ϕ_B) can also be calculated from C-V measurements using the following equation:

$$\phi_{B(C-V)} = V_{bi} + k_B T ln \frac{N_C}{N_D} \qquad 3.13$$

where N_C is the effective density of states in the conduction band of 4H-SiC and is taken equal to 1.6×10^{19} cm^{-3} [62].

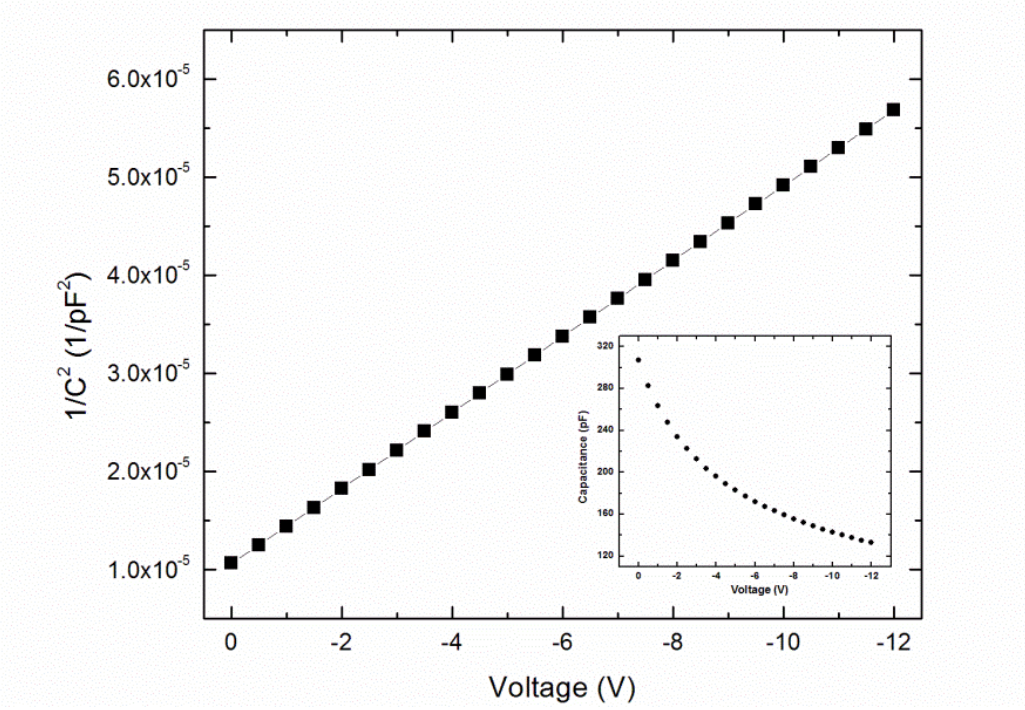

Figure 3.3 $1/C^2$ vs V characteristic of 20 μm epilayer 4H-SiC/Ni Schottky detector, at 300 K, under dark. The Inset shows the actual C-V plot.

Figure 3.3 shows a Mott-Schottky plot ($1/C^2$ vs V plot) obtained for a 20 μm n-type 4H-SiC epitaxial Schottky detector at 300 K. From the slope of the linear plot and using Equation 3.12, effective carrier concentration was determined to be 2.9×10^{14} cm^{-3}. From the extrapolation of the plot to where it intersects the voltage axis, the built-in potential V_{bi} was determined to be 1.67 V. The barrier height calculated from the C-V measurements using Equation 3.13 is 1.35 eV, which is slightly higher than the value of 1.13 eV obtained from the forward I-V characteristics. The barrier height value determined from C-V characteristic gives an average value for the whole diode [61], [80] whereas the barrier-height value obtained from forward I-V characteristics is for surface barrier height which is affected by inhomogeneity due to presence of defect centers. The higher built-in potential can be explained by the presence of a thin oxide layer at the metal-semiconductor interface, which introduces an additional small series capacitance [18] - [20], [81] – [82].

3.5 Defect Study by Deep Level Transient Spectroscopy

The current-voltage and capacitance-voltage measurements showed evidence of non-uniform barrier height due to the presence of defect centers, which can act as trap or recombination centers and may lead to incomplete charge collection. The defects characterization was carried out by deep level transient spectroscopy (DLTS) using the capacitance mode of a SULA DDS-12 DLTS system that consists of a Janis VPF-800 LN2 cryostat, a pulse generator, a 1 MHz oscillator, a correlator module, a Lakeshore LS335 temperature controller, and a high-sensitive capacitance meter. The detector was kept under a steady state reverse bias of 2 V and was pulsed to 0 V every 5 seconds with a period of 1 s to fill the traps within the depletion region.

After each time the pulse ended, thermal emission of the trapped charges caused capacitance transients and then relaxed into equilibrium. A set of correlators (10 ms, 20 ms, 50 ms, 100 ms) were applied with scanning temperature range of 84 K to 750 K, which was controlled at a heating rate of 0.05 Ks^{-1}. To be able to capture the shallow levels completely, a smaller set of correlators within a confined temperature range is needed. For this purpose, another DLTS spectra from 84 K to 140 K was conducted using 0.2 ms, 0.1 ms, 0.05 ms, 0.02 ms delays as the correlator set.

A capacitance-DLTS (C-DLTS) spectrum is generated from the temperature dependent capacitance transients followed by a saturated trap filling pulse applied to a semiconductor junction. In C-DLTS mode, the thermally activated emission rate, e_n, can be expressed as:

$$e_n = (\sigma_n \langle V_{th} \rangle N_C / g)\, exp(-\Delta E / k_B T) \qquad 3.14$$

where σ_n = carrier capture cross section,

$\langle V_{th} \rangle$ = mean thermal velocity,

N_C = effective density of states,

g = degeneracy of the trap level and was considered to be equal to 1,

ΔE = energy separation between the trap level and the carrier band,

k_B = Boltzmann constant (8.62×10^{-5} eV/K), and

T = absolute temperature

The relationship between emission rate and the capacitance transient is given by:

$$C(t) = C_o + \Delta C \exp(-te_n) \qquad 3.15$$

where C_0 is the junction capacitance at steady-state reverse bias voltage, ΔC is the difference in capacitance change measured within the rate window. The trap concentration N_t can be calculated using the following expression:

$$N_t = 2\left({}^{\Delta C(0)}/_{C}\right) N_d \qquad 3.16$$

where $\Delta C(0)$ is the difference in capacitance change between the two edges of the filling pulse and N_d is doping concentration. The peak position in DLTS spectroscopy depends on the rate window, τ, which is defined by an initial delay set for the emission rate calculations following the termination of the filling pulse:

$$Initial\ delay\ (ms) = {}^{1}/_{(4.3 \times \tau)} \qquad 3.17$$

Obtained DLTS spectra is shown in Figure 3.4. Five distinct negative peaks appeared at different temperatures corresponding to different defect levels indicating majority carrier (electron) traps. The activation energies (ΔE) corresponding to the energy separation between the trap level and the conduction band was calculated for each defect level from the Arrhenius plots ($T^2/e_n\ vs\ 1000/T$) shown in Figure 3.5. Using the Equation 3.16, the concentration (N_t) of each defect level was determined. The capture cross-section ($\sigma_{n,}$), which determines if a defect may act as a trap or recombination/generation center is also determined from the DLTS scans. Table 3.1 shows the deducted peaks, associated defect parameters, and the possible trap levels they correspond.

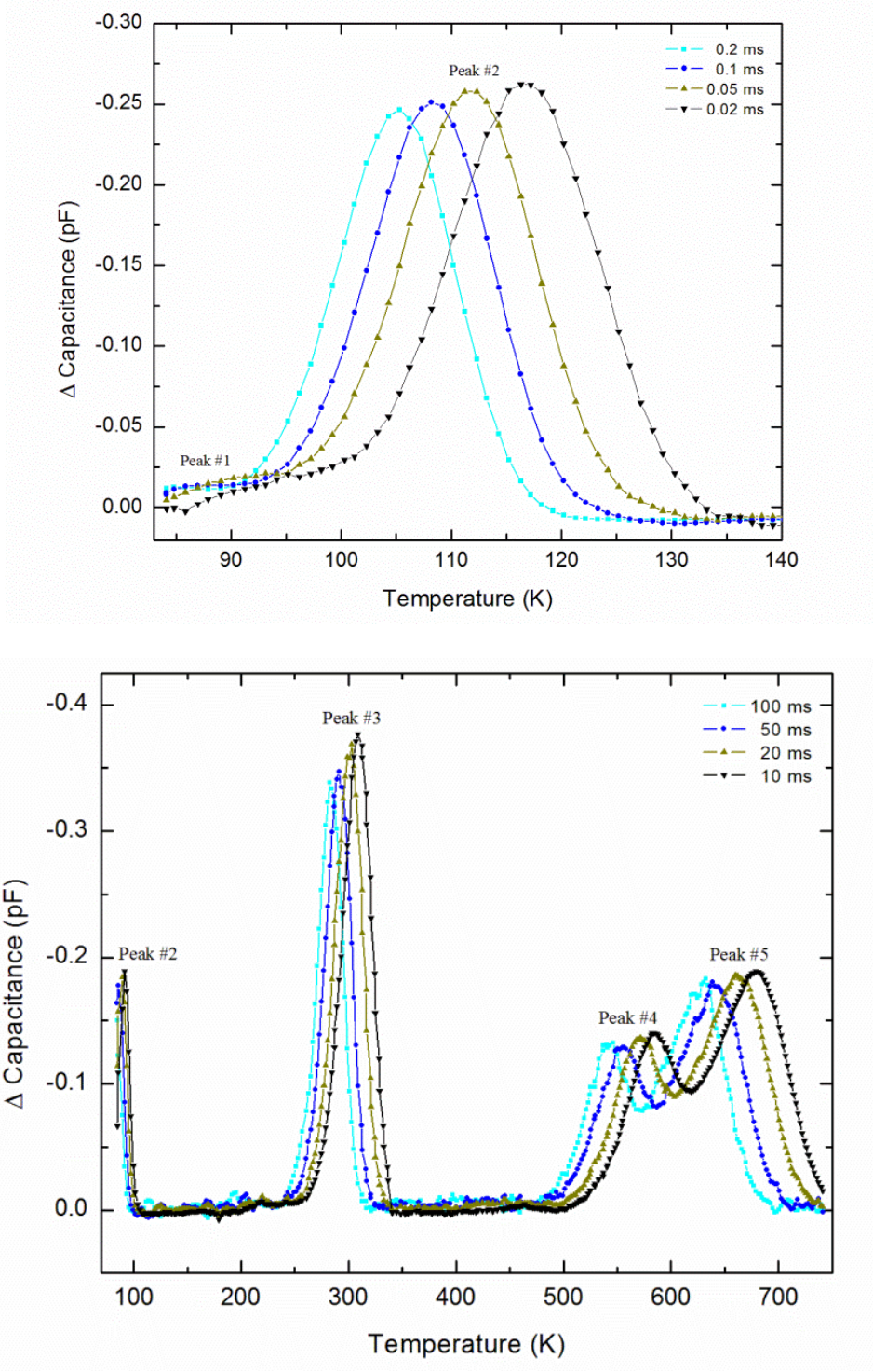

Figure 3.4 DLTS spectra obtained using n-type Ni/4H-SiC epitaxial (20 μm) detector: at a temperature range of 84 to 140 K using a smaller set of initial delays (top) and at 84 to 750 K using a larger set of initial delays (bottom).

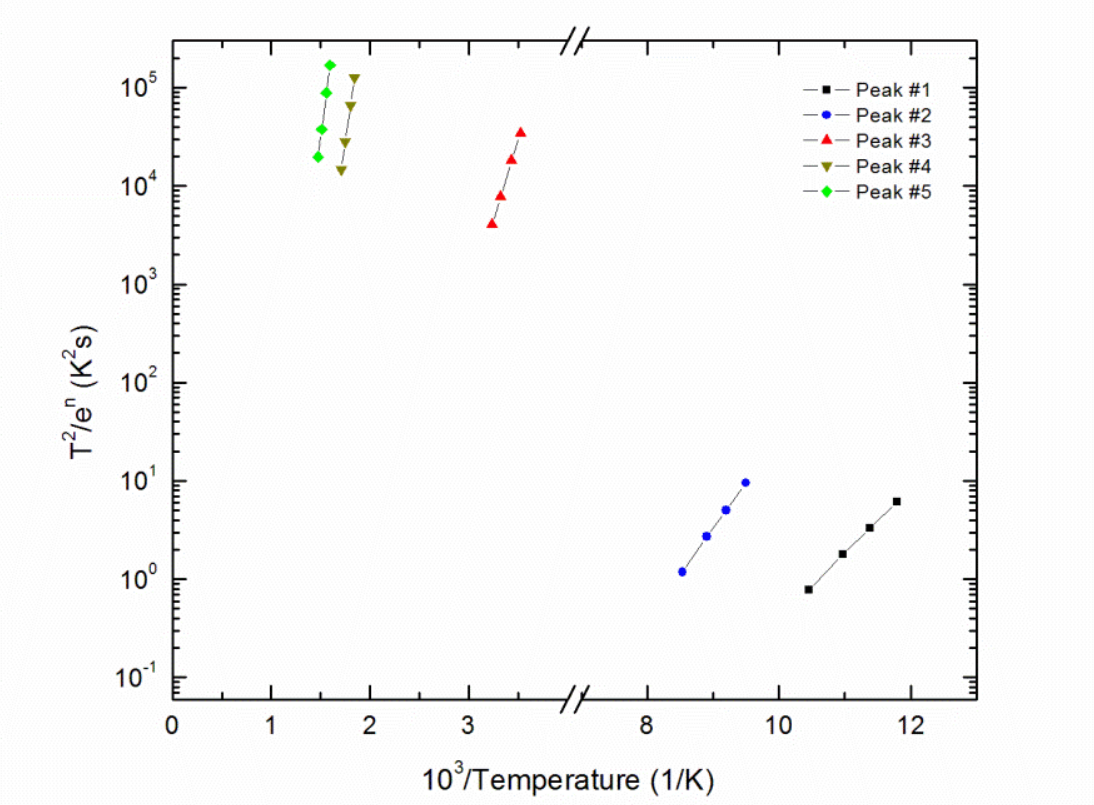

Figure 3.5 Arrhenius plot for all the peaks obtained from the DLTS scans.

Table 3.1 Defect parameters obtained from the DLTS measurements

Peak #	**σ (cm^2)**	**ΔE (eV)**	**N_t (cm^{-3})**	**Possible Trap Identity**
Peak #1	4.83×10^{-15}	E_c - (0.14 ± 0.01)	1.61×10^{11}	Ti(h)
Peak #2	9.69×10^{-15}	E_c - (0.18 ± 0.01)	2.05×10^{12}	Ti(c)
Peak #3	5.09×10^{-16}	E_c - (0.62 ± 0.02)	2.92×10^{12}	$Z_{1/2}$
Peak #4	2.16×10^{-14}	E_c - (1.42 ± 0.04)	1.08×10^{12}	EH_6
Peak #5	1.50×10^{-15}	E_c - (1.52 ± 0.03)	1.61×10^{12}	EH_7

The activation energy for trap levels in Peak #1 and Peak #2 were found to be E_c - 0.14 eV and E_c - 0.18 eV, respectively. These shallow level defects are titanium (Ti)

related substitutional impurities. These impurities come from the growth process and caused by the Ti growth reactor parts [83]. Dalibor et al. has attributed these defects to Ti^{3+} residing at cubic and hexagonal Si lattice sites [78]. Zhang et al. also assigned defect level located at E_c - 0.16 eV as Ti electron trap [77]. Castaldini et al. assigned trap level located at E_c - 0.17 eV as chromium or titanium impurities (acceptor like) in hexagonal position [84].

The Peak #3 found at 0.62 eV below the conduction band edge is due to carbon related vacancies and is identified as $Z_{1/2}$ centers. Several research groups have reported the presence of this defect level in n-type 4H-SiC and attributed the origin of such defect from silicon and carbon vacancy complexes (V_{Si}+V_C) or antisite complexes (Si_C+C_{Si}) [78], [85] – [89]. $Z_{1/2}$ center is reported to be an electrically active defect responsible for the reduction of carrier lifetime, which is detrimental to detector performance [83], [89].

The Peak #4 and peak #5, which are located at E_c-1.42 eV and E_c-1.52 eV, respectively, are related to carbon vacancies or carbon-silicon di-vacancies [11], [12], [85], [90] - [93]. They are resolved levels of $EH_{6/7}$ peak and identified as EH_6 and EH_7 trap levels.

3.6 Summary of Ni/4H-SiC Detector Characterization

20 µm *n-type* epilayer 4H-SiC detectors exhibited high Schottky barrier height and an excellent current rectification with low leakage current of ~1 nA at a reverse bias of -170 V. Current-Voltage (I-V) measurements at 300 K showed barrier height and diode ideality factor of ~1.14 eV and 1.19, respectively. The obtained barrier height was high enough to offer very good rectification properties. Capacitance-Voltage (C-V) measurements revealed a doping concentration of 2.9 x 10^{14} cm^{-3}. The I-V and C-V

measurements showed evidence of non-uniform barrier heights due to inhomogeneity indicating presence of defect centers in the detector active volume. From DLTS measurements, 5 defect levels (shallow and deep) were detected and identified as Ti(h) at E_c - (0.14 ± 0.01) eV, Ti(c) at E_c - (0.18 ± 0.01) eV, $Z_{1/2}$ at E_c - (0.62 ± 0.02) eV, EH_6 at E_c - (1.42 ± 0.04) eV, EH_7 at E_c - (1.52 ± 0.03) eV respectively. The origin of the Ti related defects are the substitutional impurities at hexagonal and cubic Si lattice sites, $Z_{1/2}$ defects are caused by interstitials and carbon vacancies, resolved levels of $EH_{6/7}$ (EH_6 and EH_7) are related to carbon vacancies and carbon-silicon di-vacancies. Low-leakage current and low-defect bearing 4H SiC detectors were then chosen for performance evaluation with alpha-radiation source.

CHAPTER 4

DETECTOR EVALUATION USING PULSE-HEIGHT SPECTROSCOPY

4.1 OVERVIEW

The performance of 4H-SiC detectors were evaluated in terms of energy resolution of the detection peak obtained by pulse-height spectroscopy (PHS). Detector response to alpha particles was evaluated using 0.1 μCi ^{241}Am alpha source which provides low-energy gamma-rays at 59.6 keV or alpha particles at 5.486 MeV. The energy resolution was calculated as full width at half maximum (FWHM) of the alpha energy peak using Gaussian peak fitting function. The collected spectrum was converted from bins to energy by adopting an absolute calibration approach developed using LabVIEW and MATLAB programming languages [4], [5], [7]. Charge collection efficiencies (CCE) were measured as a function of bias voltage for 5.48 MeV alpha particles. Using the experimentally obtained CCE values and a minority carrier diffusion model, contribution of hole diffusion to the charge collection efficiency values and the hole diffusion length has been numerically calculated. Digital spectroscopic methods were adopted to obtain the rise-time of pulses. Finally, to monitor the electronic noise associated with the detector and detection electronics, we have carried out noise analysis based on an equivalent noise charge (ENC) calculation model.

4.2 EXPERIMENTAL SETUP

When 4H-SiC radiation detectors are irradiated with ^{241}Am alpha source, incident ionizing radiations (alpha particles) interact with the semiconductor material and generate electron-hole pairs. These generated charge carriers are then swept out due to applied bias and collected at the respective electrodes giving rise to an electrical signal. The electrical signal is then converted by the front-end electronics to provide pulse-height spectra for the incident radiation. Front-end readout electronics consist of: (i) preamplifiers, which convert charge signal generated by incident alpha particles to a voltage signal; (ii) shaping amplifier, which spends a set period of time known as shaping time to filter out noise and provides a semi-Gaussian amplified output; (iii) multi-channel analyzers (MCA) which converts analog signals into digital information as pulse-height spectrum. The MCA records the height of the shaped pulse and the number of pulse-heights acquired within a given range yielding a histogram known as "Pulse-Height Spectrum". PHS depicts how many counts of radioactive photons interacted with the detector in a given energy window. Figure 4.1 shows the basic schematic diagram of the detection testing setup.

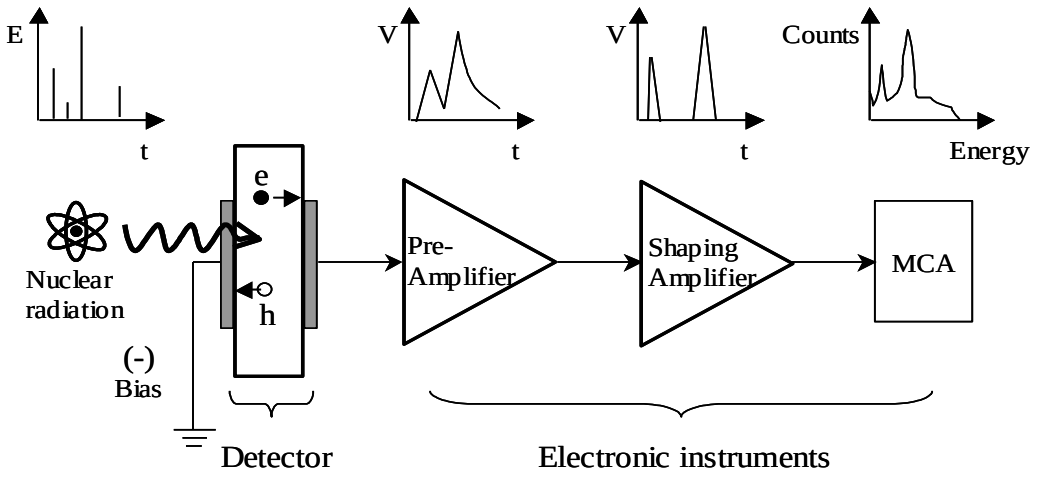

Figure 4.1 Schematic of the detector testing electronics.

For this study, the 4H-SiC detector was mounted inside an EMI shielded aluminum box, which was constantly evacuated using a mechanical rotary pump to keep the detector under a vacuum of $<1 \times 10^{-4}$ Torr in order to minimize scattering of alpha particle with air molecules. A monoenergetic 0.1 μCi ^{241}Am alpha was placed directly on top of the detector. This was a broad window source which implies that the whole surface of the detector was uniformly illuminated. An Amptek CoolFet A250CF charge sensitive preamplifier and an Ortec 671 Spectroscopy Amplifier were used to collect the detector signals. The amplified signals were then digitized and binned to obtain pulse-height spectra using a Canberra Multiport II ADC-MCA unit controlled by Genie 2000 interface software. A Canberra Multiport II ADC-MCA unit was utilized to count the shaped signal and to acquire the pulse-height spectra of the radiation detector. The peaks obtained in various spectra were fitted using peak analyzer function of Origin 8.6. Charge collection efficiencies (CCE) were measured using the same alpha source at different reverse bias voltages as the ratio of energy deposited in the detector to the actual energy of particles (5.48 MeV) emitted by the source. The energy deposited was calculated from the alpha peak position in a calibrated MCA.

Digital spectroscopic measurements were accomplished using a GWInstek (GDS1062A) digital oscilloscope used as a digitizer with a sampling rate of 1 Ms/sec and 8 bit ADC resolution. The pre-amplifier pulses were digitized and recorded in a PC for offline analysis. At least 5000 pulses were recorded to obtain a decent statistics. The data acquisition and the offline analysis software were designed in-house using the LabVIEW and MATLAB programming languages, respectively. The analyses involved calculation of

the 10 – 90 % rise-time of the charge pulses and pulse-height determination after shaping the pre-amplifier signal. The Gaussian shaping of the pulses were achieved using a transfer function resembling CR-RC^4 semi-Gaussian configuration. The software was also used to obtain distributions of pulse-height and rise-time and biparametric plots to investigate any type of correlation between the pulse-heights and pulse-shapes of a set of events.

To calibrate the system, a precision pulser, which generates waveforms and simulates the output of a radiation detector, is connected to the detection system through a capacitor. By injecting pulses of various known amplitudes (V_{pulser}, mV), energy of the charge pulses from the capacitor, E_{pulser} (in keV) is determined by the following expression:

$$E_{pulser} = \frac{V_{pulser} \times \varepsilon \times C}{1.6 \times 10^{-19}} \qquad 4.1$$

where ε is the electron-hole pair creation energy (7.7 eV for 4H-SiC). A graphical plot between E_{pulser} and the corresponding MCA peak positions of different pulse-heights gives the calibration graph. The linear plot of the peak centroid ("center of mass" of an energy peak) channel number against the pulser energy in keV gives the required calibration parameters [7].

4.3 Pulse-Height Measurements with ^{241}Am Alpha Source

Response of Ni/4H-SiC Schottky detectors fabricated on 20 μm epitaxial layer was evaluated by irradiating the detector with 0.1 μCi ^{241}Am source (peak energies: 60 keV for γ and ~ 5.5 MeV for α particles) at room temperature (~300 K). The source kept at a distance of 1.5 cm from the detector. Detector performance was evaluated in terms of energy resolution of the detection peak obtained by PHS (Figure 4.2). The energy resolution was calculated as full width at half maximum (FWHM) of the alpha energy peak

using Gaussian peak fitting function. The energy resolution of the detector was calculated by the following equation:

$$\%\ Energy\ Resolution = \frac{FWHM\ (keV)}{Incident\ Energy\ (keV)} * 100\% \qquad 4.2$$

where the incident energy is the centroid (center of the mass) of the energy peak in keV observed in the pulse-height spectrum. Lower values of energy resolution and FWHM indicate better detector performance.

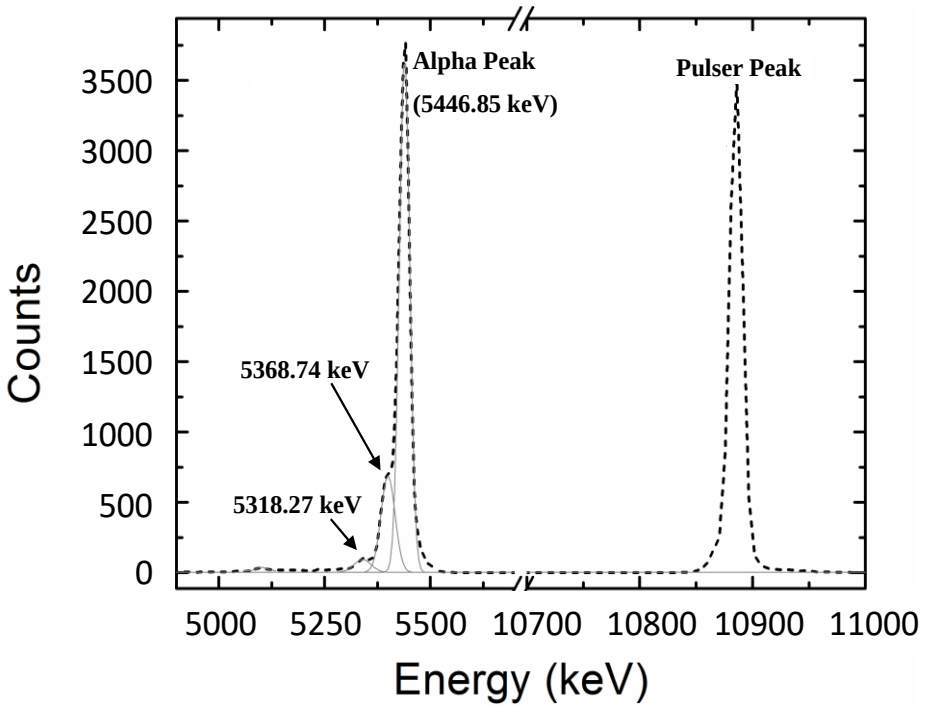

Figure 4.2 Alpha pulse height spectrum of the fabricated 4H-SiC epitaxial (20 μm) Schottky detector at an applied bias of -170 V and a shaping time of 6 μs using 1 μCi ^{241}Am alpha source. The solid lines show the deconvoluted alpha peaks, which were partially resolved.

The energy resolution was found to be ~ 0.38% for 5486 keV alpha particles incident on the detector through the 10 nm thick Ni window. This spectrum completely vanished and counts became background noise when a piece of A4 white copying paper was placed in between the radiation source and detector, confirming the detector's response

to alpha particles. By comparing response with gamma radiation, it is clear that the peak is the distinctive signal of α-radiation. The centroid of the observed peak was slightly less than the characteristic main energy peak of 5486 keV. Since a broad alpha source was used, a portion of the charged particles incident on the Ni window will scatter depending on angle of incidence and thickness of the Ni window. An improvement of the detector performance is expected if the source is collimated and metal contact thickness and material selection is optimized.

4.4 Charge Collection Efficiency

During interaction with detector material, incident alpha particles excite outer shell electrons of semiconductor atoms to a higher energy band generating electron-hole pairs (charge carriers), which are separated under applied electric field, and collected by respective electrodes producing current signal. Resolution of a radiation detector is a function of collected charge carriers generated by alpha particles, thus charge collection efficiency (CCE) provides an important measure of detector performance. Experimentally, CCE is calculated as the ratio of energy deposited in the detector (E_v) to the actual energy of the alpha particles (5.48 MeV) emitted by the source (E_0) given by:

$$CCE_{observed} = E_v/E_0. \quad (4.3)$$

The energy deposited is calculated from the alpha peak position in a calibrated MCA. Charge carriers produced in the depletion region and neutral region both could contribute to detector signal (Figure 4.3). The charge collection efficiency in theory is the sum of two contributions – CCE_{drift} and $CCE_{diffusion}$ [79]. CCE_{drift} is the contribution of charge carriers generated within the depletion region and drifted to collecting electrode.

$CCE_{difussion}$ is the contribution of charge carriers generated in the neutral region behind the depletion region and diffused to the depletion region.

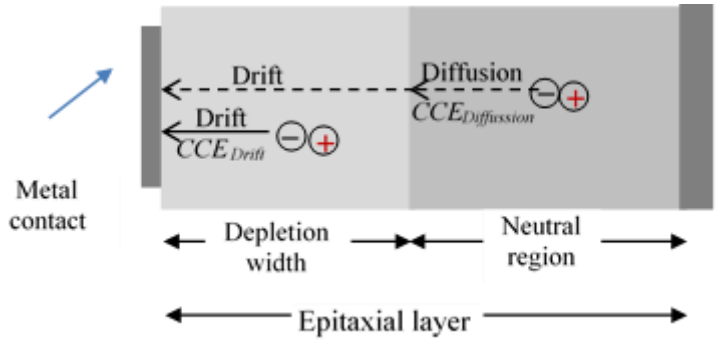

Figure 4.3 Schematic of drift-diffusion movement of charge particles in detector material; charges generated in depletion region get collected efficiently by drift, whereas charges generated in neutral region first need to diffuse to depletion region to get collected.

These two types of charge collection efficiency could be determined separately using drift-diffusion model as described in the following equations:

$$CCE_{drift} = \frac{1}{E_p}\int_0^W \left(\frac{dE}{dx}\right) dx \tag{4.4}$$

$$CCE_{diffusion} = \frac{1}{E_p}\int_W^{x_r} \left[\left(\frac{dE}{dx}\right) \times \exp\left\{-\frac{x-W}{L_d}\right\}\right] dx \tag{4.5}$$

$$CCE = CCE_{drift} + CCE_{diffusion} \tag{4.6}$$

where E_p = energy of the alpha particles,

W = depletion width at the particular bias

x_r = projected range of the alpha particles with energy E_p

L_d = diffusion length of the minority carriers, and

$\frac{dE}{dx}$ = electronic stopping power of alpha particles calculated using SRIM software.

Although charge carriers generated in both regions - depletion and neutral - could contribute to CCE, probability of collection is generally higher for charges generated within the depletion region (space charge region) compare to charges generated in the neutral region. Thus a sufficiently large depletion width, which defines the active volume within the detector, is also another crucial requirement for obtaining high energy-resolution and high efficiency detection. The width of the depletion region, *W,* for a Schottky barrier diode is dependent on the effective doping concentration (N_D) of the semiconductor material and applied bias voltage. It is mostly negligible at forward bias, but increases with applied voltage at reverse bias. Width of the depletion region can be expressed as:

$$W = \sqrt{\frac{2\varepsilon\varepsilon_0(V_{bi} - V)}{eN_D}} \qquad 4.7$$

where ε = dielectric constant of the semiconductor; which is ~9.72 for 4H-SiC,

ε_0 = permittivity of vacuum,

e = electronic charge (1.6×10^{-19} C),

N_D = effective doping concentration

V_{bi} = built-in potential and

V = Applied bias.

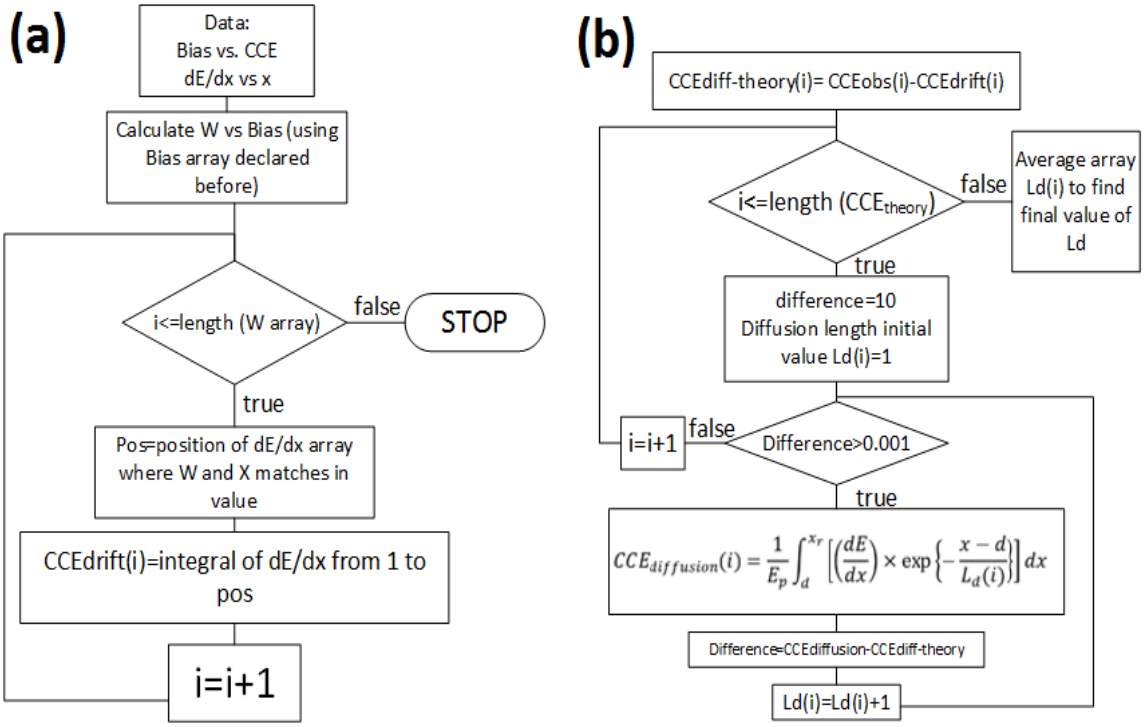

Figure 4.4. Flowchart of the Matlab based code to calculate (a) CCE_{drift}, (b) $CCE_{diffusion}$ and diffusion length L_d.

Figure 4.4 shows the flowcharts of the developed MATLAB based code to calculate the CCE_{drift} and $CCE_{diffusion}$ using L_d as a free parameter. The process started by obtaining the depletion width (W) values as a function of the applied bias. In order to integrate the dE/dx array in terms of dx, it was necessary to find the position of the array where the depletion region (W) and the x array match. This process was repeated for each value of the depletion width and which returned the CCE_{drift} values at a particular bias voltage. The CCE_{obs} (observed charge collection efficiency) was calculated as the ratio of the output energy observed by the detector to the actual incident energy of the alpha particles (5.48 MeV). Implementing the MATLAB based program and using drift-diffusion model (Equations 4.4 - 4.6), total charge collection efficiency (CCE_{total}), collection efficiency in depletion region (CCE_{drift}), and collection efficiency in neutral region ($CCE_{diffusion}$)

were determined separately with varying applied bias under 5.48 MeV alpha particles irradiation.

Figure 4.5 compares different CCE values with varying reverse bias voltages. At lower bias the depletion width was smaller than the alpha penetration depth in 4H-SiC (18 μm), and most of the charge carriers were generated in the neutral region and minority carrier has to diffuse to depletion region to get collected. As the applied reverse bias increases, width of depletion region increases allowing more number of generated electron-hole pairs to contribute toward CCE_{drift}, thereby increasing total CCE. Total CCE improves with applied reverse biases up to a reverse bias of about 85 V, then levels off. At this point, charge collection is almost solely due to carrier drift inside the depletion region (CCE_{drift}). Any electron-hole pairs generated by the alpha particle outside of the depletion region do not contribute significantly toward total charge collection efficiency.

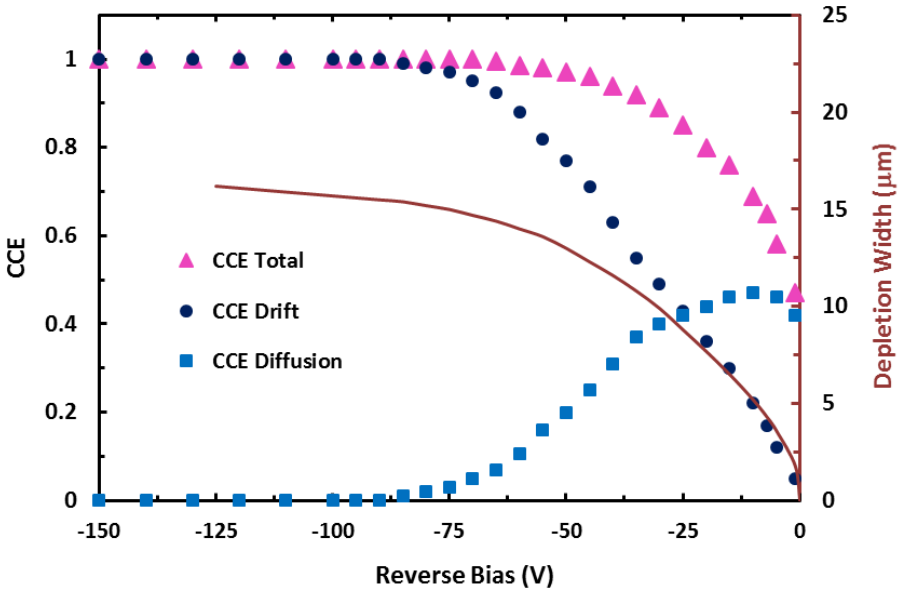

Figure 4.5 Variation of total CCE as a function of reverse bias voltage. CCE from drift and diffusion are calculated separately using drift-diffusion model. Variation in depletion width are also shown.

Alpha particles of 5.48 MeV energy have a projected range (penetration depth) of 18 μm in SiC. The depletion width in the fabricated detector was calculated to be ~ 15 μm at a reverse bias of 85 V. So the alpha particles did not deposit their full energy within the depletion region which is the active region of the detector. This suggests although theoretically 100% collection efficiency should be achieved at a reverse bias of 85V, in reality a lower value of CCE was attained. Experimentally, the highest CCE achieved was 92 %. A CCE value less than 100% also suggests that a fraction of the generated charge carriers are getting trapped and eventually lost (recombine) in the defect centers. The energy resolution increased with the increment in the bias due to the increased CCE at higher bias. At biases beyond - 85 V, the performance of the detector gets almost saturated, and experimental results indicated that the best resolution was obtained at - 90 V.

4.5 Electronic Noise Analysis

It is critical to control electronic noise in signal processing by front-end readout electronics as noise introduced in this stage can significantly affect the resulting pulse-height spectrum and thereby detector resolution. The charge signal generated in the detector requires amplification to a voltage signal by a preamplifier. A field effect transistor (FET) is used at the input of the high-gain amplifier. Equivalent noise charge (ENC) consists of contribution of different noise sources that influence in the radiation detection signal acquisition and processing. For ENC analysis, pulse-height spectra were recorded using the precision pulser generating pulses at a fixed amplitude and frequency. The electronic noise was measured from the pulser peak width and expressed in terms of ENC in charge units. ENC noise components were calculated using the formalism developed by Bertuccio and Pullia [79] where ENC is expressed as:

$$ENC^2 = (aC_{tot}^2 A_1)\frac{1}{\tau} + \left[\left(2\pi a_f C_{tot}^2 + \frac{b_f}{2\pi}\right)A_2\right] + (bA_3)\tau \qquad 4.8$$

where C_{tot} is the total input capacitance

a = white series noise contribution from the thermal noise in the FET channel,

A_1, A_2, and A_3 = constants which depend on the response of the shaping network,

τ = shaping time,

a_f = coefficient of the FET 1/f noise,

b_f = dielectric noise coefficient, and

b = sum of the white parallel noise contribution due to the shot noise of the FET, leakage current in the detector, and thermal noise in the feedback resistor.

The ENC as a function of amplifier shaping time τ was fitted to Equation 4.8 using a least square estimation method implemented with MATLAB coding [42] in order to calculate the three components – (i) white series noise, , which is primarily due to the total input capacitance, (ii) white parallel noise, and (iii) pink noise (f parallel and $1/f$ series). As expected, the noise components were higher when the biased detector was connected to the system compared to the noise with preamplifier only. The data revealed that the contribution of the white series noise dominate over the white parallel and the pink noise. At a given shaping time, following connection of the detector, the white series noise increased by an order of magnitude, the white parallel noise increased by a factor of ~5, and the pink noise increased marginally as it is independent of shaping time. The increase in white series noise is due to increase in the input capacitance from the detector. The increase in white parallel noise results from the additional current from the detector due to

charge carrier generation. The minimum ENC for the biased detector under irradiation was observed at a shaping time of 3 μs.

4.6 BIAS DEPENDENCE OF EQUIVALENT NOISE CHARGE

In order to study the effect of detector leakage current on the electronic noise, a bias dependent study of the electronic noise was carried out. The ENC was measured at seven different reverse bias voltages viz. -20, -40, -60, -80, -100, -120 and -140 V. Figure 4.6 shows the variation of ENC and the separate noise contributions to the overall ENC as a function of applied reverse bias at an optimized shaping time of 3 μs. Increasing reverse bias reduces the detector junction capacitance and increases leakage current. The contribution of the dominating white series noise decreased with the increasing reverse bias. The pink noise followed a similar trend. The white parallel noise, which incorporates the detector leakage current, contributed the least at lower biases and increased steadily with reverse bias due to the increase in leakage current. It can be noticed that beyond a bias of -80 V, the contribution of the white parallel noise exceeded that of the pink noise.

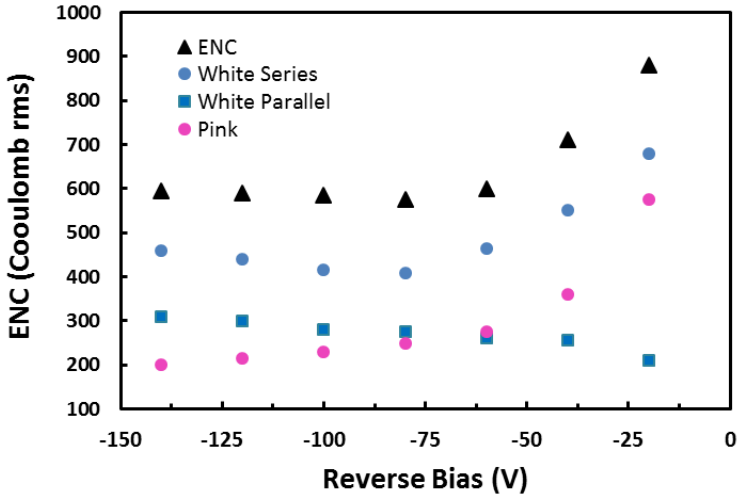

Figure 4.6 . Variation of equivalent noise charge (ENC), white series noise, white parallel noise, and pink noise measured using 3 μs shaping time, as a function of different bias voltages.

4.7 CONCLUSION

Performance of alpha particle detectors fabricated on 20 μm thick 4H-SiC n-type epitaxial layers was evaluated using pulse-height spectra (PHS) produced under a 0.1 μCi ^{241}Am alpha source. The pulse-height spectra showed clearly resolved peaks for three major alpha particle energies – 5388 keV, 5443 keV, and 5486 keV emitted from an ^{241}Am source at 170V reverse bias. The energy resolution was calculated as full width at half maximum (FWHM) of the alpha energy peak using Gaussian peak fitting function. An energy resolution of ~0.38% was observed for 5486 keV alpha particles with this detector. The high resolution was achieved by using high quality epitaxial layers which provided less doping concentration, a micropipe density less than 1 cm^{-2} and Schottky barriers with high barrier height and diode ideality factor close to 1.

Using a precision pulser, which generates waveforms and simulates the output of a radiation detector, charge collection efficiency (CCE) was determined as a function of bias voltage. A MATLAB code was used to implement a drift-diffusion model which fits the variation of CCE with reverse bias. A diffusion length of ~13.6 μm was calculated using the drift diffusion model. A CCE of ~92% was observed for this detector, which suggests that a fraction of the generated charge carriers is getting trapped and eventually lost (recombine) in the defect centers.

An electronic noise analysis of the detection system revealed the possibility of achieving even better energy resolution by lowering the detector capacitance. The contribution of the white series noise (which is primarily due to the total input capacitance) to the overall electronic noise was found to dominate compared to the white parallel and the pink noise up to a reverse bias of -140 V and decrease steadily with decreasing

capacitance. The contribution of pink noise which is also primarily due to the total input capacitance, was seen to be more than that of the white parallel noise for bias voltages less than -80 V and beyond which the contribution of white parallel noise which incorporates the detector leakage current became more because of the increased leakage current. As a future venture, we would target lower detector capacitance without reducing the detector active area by increasing the detector active thickness, i.e. using a thicker epitaxial layer.

CHAPTER 5

IMPROVED DETECTOR PERFORMANCE BY EDGE TERMINATION

5.1 OVERVIEW

Wide bandgap semiconductor 4H-SiC has been established as a suitable material for devices operating beyond room temperature and in harsh environments. Although the desired material properties for creating excellent radiation detectors are present in 4H-SiC, there are extended and microscopic defects identified within the detector active region. These defects which were introduced during substrate and epilayer growth adversely affect the charge transport properties and thereby detector performance. More specifically, surface related defects with the metal-semiconductor interface and deep levels traps, radiation interaction generated electron-hole pairs before reaching the electrodes resulting in incomplete charge collection. This in turn leads to a decrease in signal-to-noise ratio and a reduction in energy resolution of the pulse-height spectra (PHS) which is a ratio between the full-width at half-maxima (FWHM) and the centroid of the peak. Consequently, there is a need for a process aimed at suppressing leakage currents and reducing the effects of deep levels by eliminating or rendering them electrically inactive.

In this Chapter, the development of an edge termination by depositing thin Si_3N_4 passivating film on 4H-SiC epilayer is presented. This technique significantly improves device leakage current and favorably affects deep levels leading to a drastic improvement

in detector performance. A comparison of the results prior to and subsequent edge termination using passivating Si_3N_4 layer on 4H-SiC epilayer Schottky barrier detectors are presented. Defect parameters are evaluated and compared with that of a similar non-edge terminated detector from the same parent wafer.

5.2 Electrical Characterization

For these experiments, a 400 nm thick Si_3N_4 passivating layer was deposited on the epilayer surface surrounding the Ni Schottky contact of a 4H-SiC detector grown on 20 μm thick n-type epitaxial layer. The fabrication of such detector is described in detail in Chapter 2. The electrical properties of edge terminated Schottky barrier diodes were studied by current-voltage (I-V) and capacitance-voltage (C V) measurements in an EMI-shielded aluminum box at room temperature.

Figure 5.1 shows the I-V characteristics under forward and reverse bias at room temperature prior to and subsequent Si_3N_4 edge termination. The leakage current was found to have reduced two orders of magnitude from 4.5 nA to 86 pA following edge termination. Effective surface barrier height and diode ideality factor were determined from the forward I-V characteristics by applying a thermionic emission model as discussed in Chapter 3. Schottky barrier height was found to improve significantly after Si_3N_4 edge termination and was high enough to show very good rectification properties as seen in the reverse I-V characteristics of Figure 5.1. The diode ideality factor did not vary significantly and was determined to be near unity, which suggests spatial uniformity of the barrier height across the Schottky contact surface area. C-V measurements were carried out in a bias range of -15 to +15 V, and a change in the capacitance value in this bias range was ~ 1pF for the detector with edge termination. The capacitance value obtained for 4H-SiC detector with

Si_3N_4 passivating layer was lower by an order of magnitude compared to the detector without passivating layer.

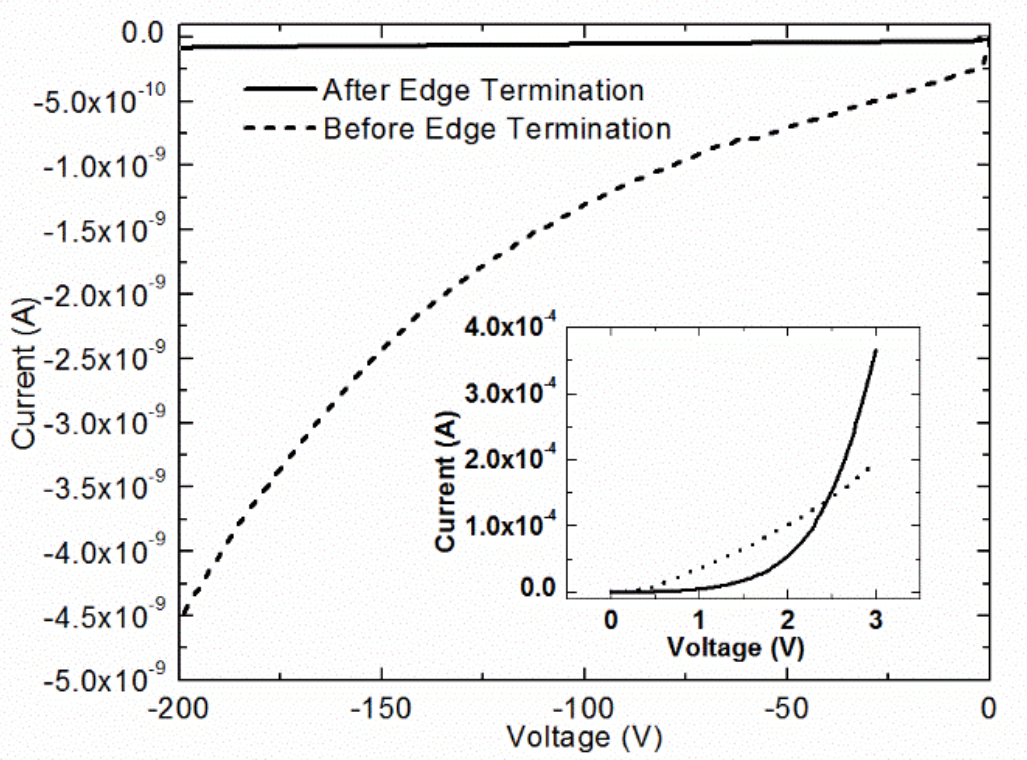

Figure 5.1 I-V characteristics from before and after Si_3N_4 edge termination of a 4H-SiC Schottky barrier radiation detector. Inset shows forward I-V characteristics.

5.3 Pulse Height Spectroscopy

Pulse height spectroscopy was carried out in an EMI shielded aluminum sealed box with a standard broad window 0.1 µCi ^{241}Am alpha source mounted above the detector. A charged sensitive Amptek A250CF preamplifier was used to collect the detector signals. The incoming signals were shaped by an Ortec 671 Spectroscopy Amplifier. The amplified and shaped signals were collected using a Canberra Multiport II ADC-MCA unit to obtain the pulse-height spectra. The energy resolution was expressed in terms of full width at half maximum (FWHM).

Figure 5.2 compares alpha spectroscopy measurements of the detector before and after Si_3N_4 edge termination using a ^{241}Am source. The measurements were carried out at room temperature with an applied bias of -120 V. The results showed that after Si_3N_4 edge termination, the energy resolution exhibited a significant improvement from 0.55% to ~ 0.38% where the three major alpha particle energies emitted from the ^{241}Am source are clearly resolved compared with those without edge termination shown in the inset in Figure 5.2. Since a broad alpha source was used, depending on angle of incidence a portion of the incident charged particles on the Ni window will scatter. So the centroid of the observed peak was slightly lower than the characteristic energy peak of 5486 keV. This could be improved using a collimated energy source. It is evident from the convolution of the two peaks on the lower energy side of the 5486 keV line and small variation in pulser peak FWHM that the detector performance is affected by charge loss due to defects.

In 4H-SiC detector with edge termination, the Si_3N_4 layer surrounding the detector widow act to colliminate alpha particles incident on the detector widow and block particles incident outside of the widow when using a broad alpha source. This improves charge collection efficiency and reduces the broadening of the spectrum. Detector parameters obtained from electrical and spectroscopic characterization are summarized in Table 5.1.

Table 5.1 Detector parameters obtained from electrical and spectroscopic characterization

Detector ID	Ideality Factor n	Barrier Height Φ_B (eV)	Leakage Current @ -200 V (pA)	N_{eff} (10^{14} cm^{-3})	Bias (-V)	Sh. Time (µs)	Energy Resolution (%)	Pulser width (keV)
S2 (w/o Si_3N_4)	1.04	0.96	4524	2.05	120	6	0.55	15.8
S1 (w Si_3N_4)	1.02	1.34	85.8	2.42	120	6	0.38	10.3

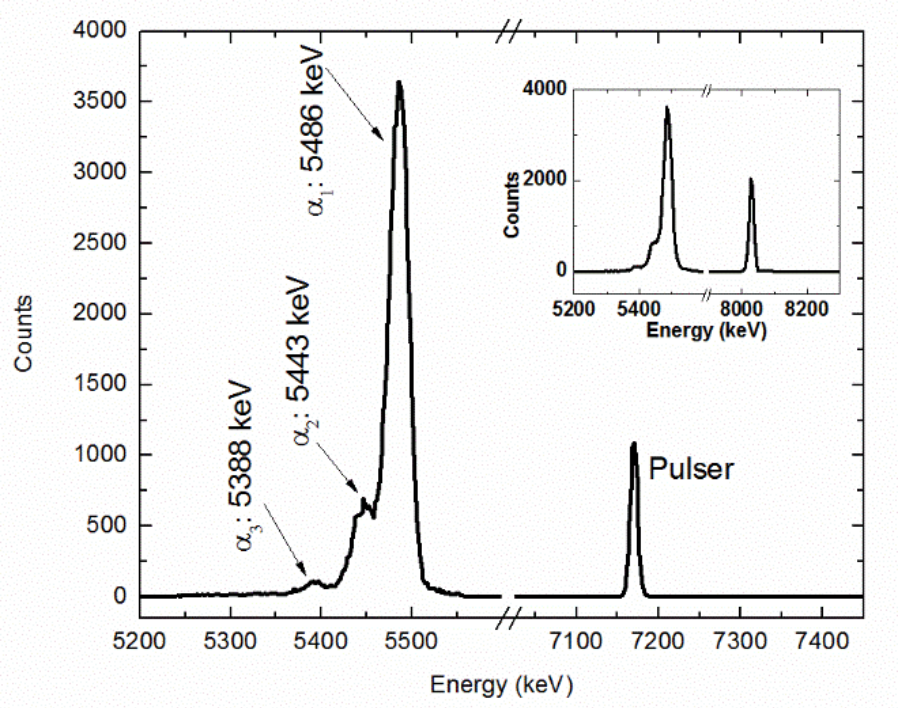

Figure 5.2 Alpha pulse-height spectrum collected prior (Inset) and subsequent to Si_3N_4 edge termination of a 4H-SiC Schottky barrier radiation detector.

5.4 Defect Characterization

Defect characterization was performed on edge terminated and non-edge terminated detectors using a SULA DDS-12 Deep Level Transient Spectroscopy (DLTS) system. DLTS scans were carried out in the temperature range from 80 K to 750 K with a steady-state reverse bias of -2 V. The detector was pulsed to 0 V with a pulse width of 1 ms followed by the capacitance transient measurements. The DLTS measurements for the Si_3N_4 edge terminated detector revealed three defect levels shown in Figure 5.3 as Peaks #1 - #3. The negative peaks suggest majority carrier traps (electron trap in this case). An additional DLTS scan (Figure 5.3-b) was performed with smaller correlator delays to fully observe peak #1. A non-edge terminated detector was fabricated from a sample adjacent to the Si_3N_4 edge terminated detector in the same parent wafer and characterized by DLTS

for comparison. Figure 5.4 shows the Arrhenius plots for the two detectors. The defect parameters viz., activation energy, capture cross-section, and the trap concentration were calculated for the two detectors and are listed in Table 5.2 where S1 is the detector with edge termination and S2 is without.

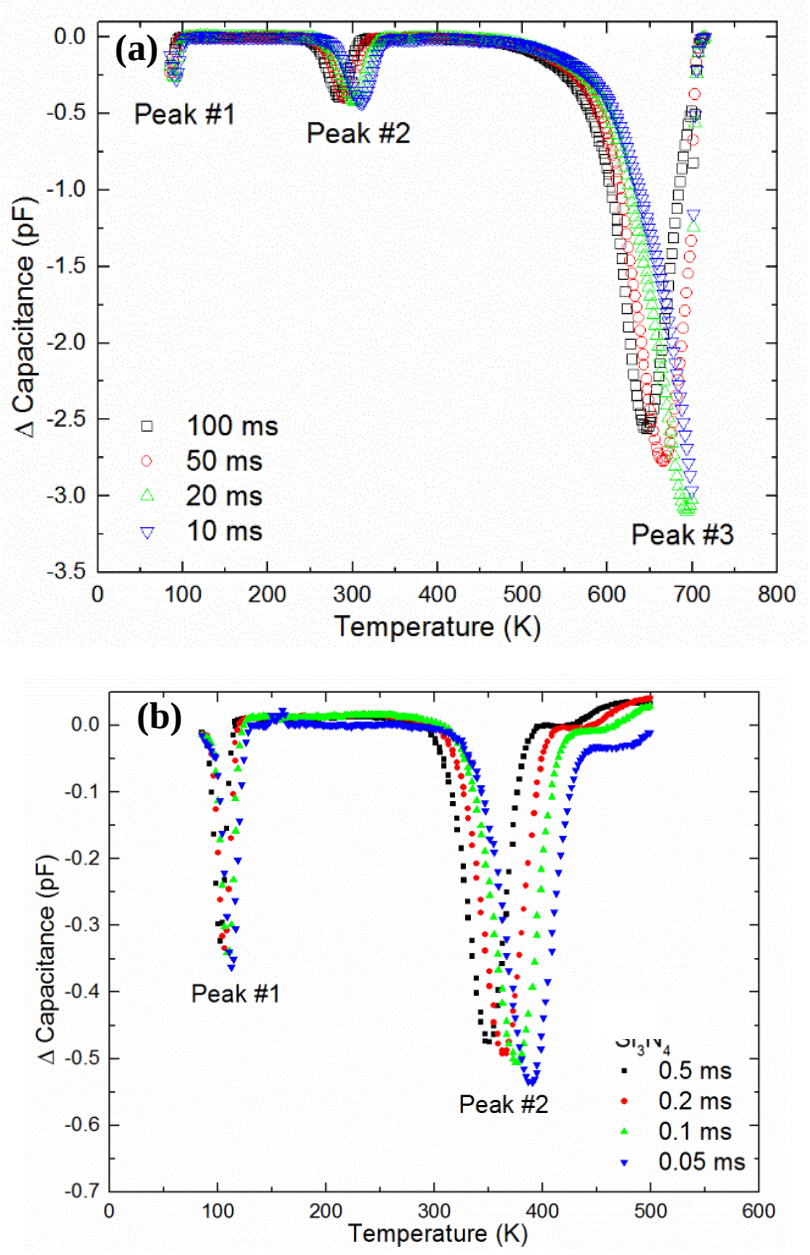

Figure 5.3 DLTS scan from 80 K to 750 K of Si_3N_4 edge terminated 4H-SiC Schottky barrier radiation detector: (a) using larger correlator delays and (b) using shorter correlator delays to fully observe peak #1.

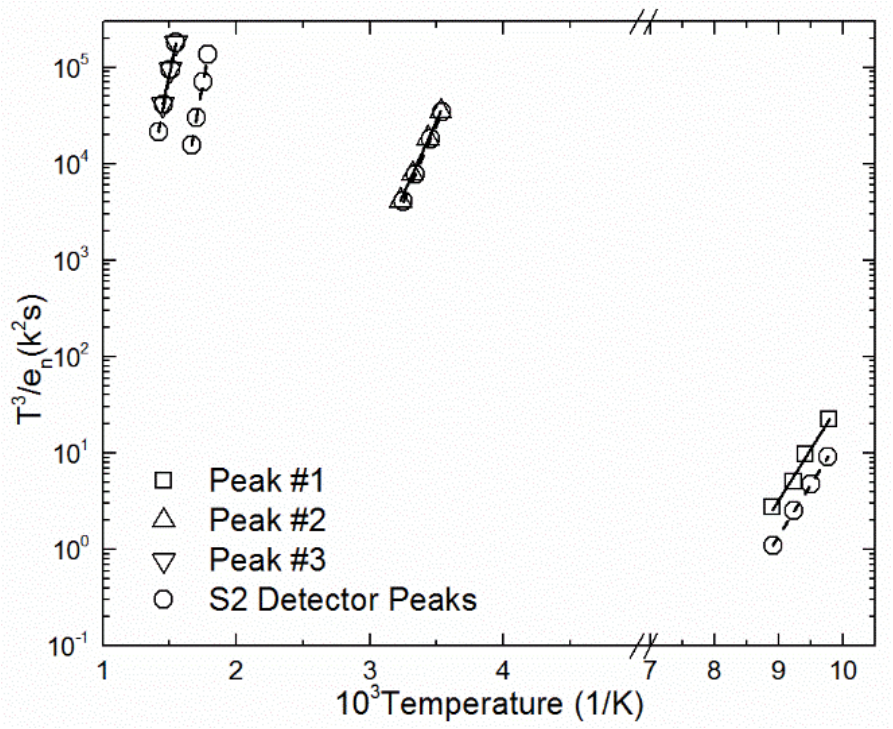

Figure 5.4 Arrhenius plot of the Si_3N_4 edge terminated detector (peaks 1-3) and a non-edge terminated detector (○) fabricated from an adjacent sample in the same parent wafer.

According to the calculated activation energy, the position for peak #1 was found to be $E_C - 0.22$ eV where E_C is the bottom of the conduction band. This shallow level defect has been identified as titanium substitutional impurity. Dalibor *et al.* have reported similar defect levels in titanium implanted 4H-SiC [78]. Peak #2 located at 0.63 eV below the conduction band edge and has been designated as electrically active $Z_{1/2}$ defects which is related to defect complexes involving equal number of silicon and carbon site vacancies as summarized by Zhang *et al.* [77]. The activation energy for the defect level corresponding to peak #3 was found to be located at 1.25 eV below the conduction band edge for which Alfieri *et al.* have reported a similar defect level for chlorine implanted n-type 4H-SiC designated by them as Ci1 [94]. In our previous work [4], [93], we have reported on two deep levels that were found to affect detector performance the most, $Z_{1/2}$ and a shouldered

peak $EH_{6/7}$. The defect level $EH_{6/7}$ represents carbon-carbon or carbon-silicon di-vacancies or related complex. The $EH_{6/7}$ was not observed in the Si_3N_4 detector during DLTS measurements, but this defect has appeared in every detector fabricated from this wafer as can be seen in Peak #3 and #4 for detector S2 listed in Table 5.2. Comparing the $Z_{1/2}$ and $EH_{6/7}$ defect levels between the two detectors, it can be concluded that Si_3N_4 edge termination had a significant effect in the reduction of the trap concentration of $Z_{1/2}$ and no detectable presence of $EH_{6/7}$ defect level. Hiyoshi et al. [95], and Kawahara et al. [96] have demonstrated the reduction of $Z_{1/2}$ and $EH_{6/7}$ defect levels by thermal oxidation and have suggested the mechanism to be the indiffusion of interstitials from the interface recombining with vacancies in the epilayer. The Si_3N_4 edge termination layer was processed at a temperature of 300˚C which is much lower than the thermal oxidation temperature (1150˚C - 1300˚C) used by Hiyoshi.

5.5 Conclusion

The effectiveness of edge termination using passivating Si_3N_4 layer was studied in terms of detector leakage current and alpha radiation detection performance. Results were compared with those of non-edge terminated detectors. Following edge termination with Si_3N_4, 4H-SiC detectors exhibited two orders of magnitude lower leakage current compared to I-V measurements taken from before edge termination. Alpha spectroscopy measurements conducted prior and subsequent to edge termination revealed a substantial improvement in terms of energy resolution. DLTS results showed a reduction in the defect densities of $Z_{1/2}$ and no detectable presence of $EH_{6/7}$ defect levels in the Si_3N_4 edge terminated detectors compared with a non-edge terminated detector from the same parent wafer. These defects play significant role in detector performance and reduction or

elimination of these defects resulted in higher charge collection thereby improved detector resolution. We suggest the C_i and Si_i atoms in participation induced stress/strain from lattice mismatch at the Si_3N_4/SiC interface layer may be responsible for the reduction of the $Z_{1/2}$ and $EH_{6/7}$ defect levels; however, further investigation is going on for correlation.

Table 5.2 Defect parameters obtained from DLTS measurements (Detector S1 is with edge termination and S2 is without)

Detector ID	Peak #1				Peak #2				Peak #3				Peak #4			
	Trap	σ_n $\times 10^{-13}$ cm^2	ΔE eV	N_t $\times 10^{12}$ cm^{-3}	Trap	σ_n $\times 10^{-16}$ cm^2	ΔE eV	N_t $\times 10^{12}$ cm^{-3}	Trap	σ_n $\times 10^{-15}$ cm^2	ΔE eV	N_t $\times 10^{12}$ cm^{-3}	Trap	σ_n $\times 10^{-16}$ cm^2	ΔE eV	N_t $\times 10^{12}$ cm^{-3}
S1	Ti(c)	4.70	0.22	2.14	$Z_{1/2}$	7.24	0.63	3.16	Cil	0.6	1.25	18.3	-	-	-	-
S2	Ti(c)	0.71	0.19	2.52	$Z_{1/2}$	5.04	0.62	4.16	$EH_{6/7}$	5.52	1.40	1.04	$EH_{6/7}$	1.73	1.45	1.34

CHAPTER 6

MULTIPIXELATED CZT GAMMA-RAY DETECTOR

6.1 OVERVIEW

$Cd_{0.9}Zn_{0.1}Te$ (CZT) based pixelated radiation detector was fabricated and characterized for gamma ray detection. CZT has inherent poor hole-transport properties compared to electrons, meaning holes are more likely to get trapped causing degradation in energy resolution. In small-pixel geometry, where the size of segmented contact electrode known as 'pixel' is smaller compared to the detector thickness, detector operates in a unipolar charge-sensing mode where observed signal is mostly due to electron transport. A 3×3 guarded pixilated detector was fabricated on a ~20×20×5 mm^3 crystal cut out from the grown ingot. A guard ring grid was used to reduce inter-pixel/inter-electrode leakage. CZT single crystal grown in our lab using a tellurium solvent method was used to fabricate the pixelated detector. The crystal was characterized in planar configuration using electrical, optical, and optoelectronic methods prior to the fabrication of pixilated geometry. Current-voltage (I-V) measurements was carried out to determine resistivity and leakage current at various operating bias voltage. Electron mobility-lifetime products ($\mu_e\tau_e$) was measured through alpha ray spectroscopy. The devices were tested for their performance as high-energy gamma ray detector using a ^{137}Cs radiation source.

6.2 SMALL PIXEL DETECTOR STRUCTURE

While CZT offers several advantages such as room temperature operation, high stopping efficiency, and compact construction, the material has a major limitation in charge transport properties as compared to elemental semiconductors like silicon and germanium. Large volume CZT detector performance is often limited by the poor charge transport properties such as low drift-mobility and short lifetime especially for holes. This limitation leads to degradation in the energy resolution and detection efficiency. Table 6.1 compares electron and hole mobility and mobility-lifetime product in CZT.

Table 6.1 Charge Transport properties of CZT

Electron Mobility, μ_e ($cm^2/V.s$)	>1000
Hole Mobility, μ_h ($cm^2/V.s$)	~50
Electron Mobility Lifetime Product, $\mu_e\tau_e$ (cm^2/V)	$10^{-2} – 10^{-3}$
Hole Mobility Lifetime Product, $\mu_h\tau_h$ (cm^2/V)	$\sim10^{-5}$

When a gamma-ray deposits energy in a semiconductor, electron-hole pairs are produced and are drifted towards appropriate electrodes due to the applied bias. However, many of these carriers get trapped before they reach the electrodes. This is especially true for holes, which move more slowly than electrons and are therefore more likely to get trapped. As a result, a significant fraction of count does not appear in the photopeak but are in the low energy tail. The charge trapping effect is more pronounced in thicker detectors as the charges require longer transit time.

Various approaches can be used to solve the problem of charge trapping. Clearly, elimination of all traps is the most direct approach. However, this is practically impossible

to achieve. The poor charge transport for the holes inherent in the CZT material can be circumvented by using modified electrode structures to operate detectors in a unipolar charge-sensing mode [97] – [99]. In this approach, the induced pulse is mostly due to electron motion in the detector and the hole contribution to the signal is negligible, thereby reducing the effect of hole trapping. Two prevalent approaches for the unipolar charge sensing methods are the reduced anode geometry [97], [100] and the coplanar electrode design [99]. While the two concepts are essentially similar in principle, the detector fabrication and electronic signal processing steps are significantly simpler in case of reduced anode geometry especially when an array is configured for an imaging application (as in the present case). As a result, small pixel geometry was selected for this current study. In this approach, the unipolar signal induction is achieved in a pixellated detector array by keeping the pixel size small as compared to the detector thickness.

Earlier work of Barrett et al [97] has demonstrated that for a segmented detector array, signal generation and pulse height spectrum characteristics depend on the ratio of the pixel size ($\in$) to the detector thickness (L). Their analysis shows that for small ($\in$/L) ratio, the overall contribution of holes to the signal and the effect of hole trapping is significantly reduced, and electron transport is primarily the mechanism for signal generation, as shown by their theoretical estimations in Figure 6.1. This is mostly because in the small pixel regime, the electrostatic coupling between the moving charge and the pixel electrode is strong only in the close vicinity of the pixel. Thus, by appropriate biasing the electrons can be collected at a pixel electrode and the resulting induced pulse is produced only when the electron is close to the pixel. Thus the effect of hole trapping on the resulting pulse height spectrum is significantly reduced. Figure 6.2 presents a schematic

of the multi-pixel CZT detector which were fabricated in clean-room facilities by photolithographic technique as well as contact mask evaporation as described in the following sections of this chapter.

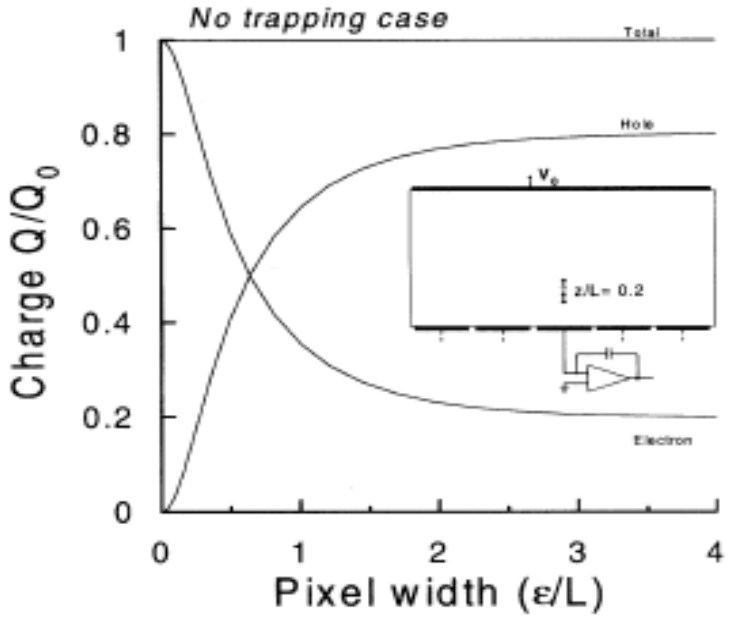

Figure 6.1 Contribution of electrons and holes to the total collected charge as a function of the pixel size. The interaction depth is 20% of the detector width (L) (Barrett et al, [97]).

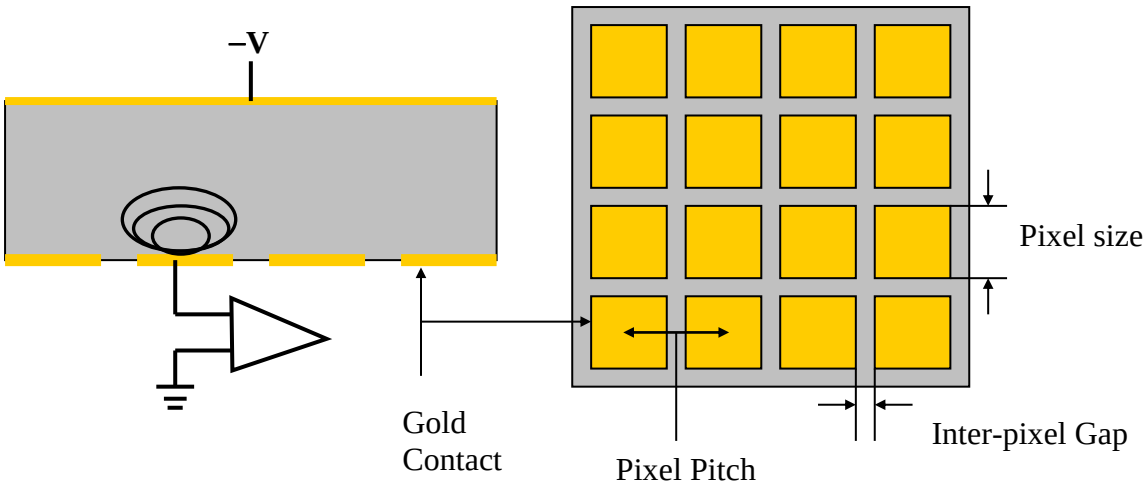

Figure 6.2 Schematic of a small pixel device showing high accumulation of weighting potential near pixel electrode. The bottom contact pattern is shown on the right.

6.3 CZT SINGLE CRYSTAL

Single crystal of CZT growth entails transformation of precursor materials from a liquid phase to the solid phase ternary CdZnTe compound in order to grow an ordered lattice structure. The growth temperature must be well above the melting point of the precursor elements as well as the compounds themselves (CdTe, ZnTe, and CZT). CZT crystal is typically grown by melt growth techniques such as Bridgman method and the travelling heater method (THM) which involve melting the precursor material, and then crystallizing the material by changing pressure, temperature, or a combination of both [50], [52] – [54]. For this study, CZT single crystals with stoichiometric ratio of $Cd_{0.9}Zn_{0.1}Te$ and grown by tellurium (Te) solvent growth technique using 50% excess Te as a solvent by our research group was used. This growth method combines many favorable features of the Bridgman method and THM growth methods. Zone refined precursor elements at a Cd:Zn:Te ratio of 30:12:58 at% were used along with indium (In, at 15-25 ppm) as a dopant.

Grown CZT crystals were cut and polished using a series of sandpapers of different grits and ultimately microfiber pads to achieve a mirror finish on all faces of CZT crystal wafers. CZT crystal wafers are then cleaned using an ultrasonicator, etched with 2% bromine-methanol solution (Br_2-MeOH) for 90 seconds, and rinsed off with de-ionized water. Optical characterizations were performed using UV-Vis-NIR spectroscopy revealing a direct bandgap energy of ~ 1.56 eV at 300K for the grown and processed wafers. IR transmission of the surface of the CZT crystal used in this study revealed an average tellurium inclusion/precipitate size of ~8 μm. Te inclusions with diameters greater than 10 μm can act as potential charge trapping centers and significantly degrade the

detector's performance [101], [102]. After crystal characterization, CZT multi-pixel nuclear detectors were fabricated on the processed wafers.

6.4 CZT Multi Pixel Detector Fabrication

Large area CZT crystal of dimensions 20×20×5 mm^3 was cut out from the grown ingot, ground, lapped (down to 1 μm SiC paper), and polished (down to 0.05 μm alumina powder in a suspension). Figure 6.3 (a) shows a bare polished 20×20×5 mm^3 crystal cut from the grown CZT ingot and ready for detector fabrication. Pixelated structure with guard rings was used as anode and was fabricated using photolithography on the Te-rich face of the crystal. Guard rings are used to reduce the noise caused by surface leakage current within a nuclear detector. A guard ring structure involves the use of an anode contact electrode, surrounded by a space where only the bare semiconductor surface exists (no contact electrode). Since the guard ring is not connected to the anode, all current caused by surface conduction are blocked by the guard ring and do not interfere with the resulting detection signal from the anode.

Figure 6.3 (b) shows the schematic of the pixelated detector showing 4 adjacent pixels and their dimensions, and Figure 6.3 (c) shows the photograph of the actual 3×3 pixelated detector used in this study. Each pixel had a dimension of 5×5 mm^2 with 1.25 mm inter-pixel gap and was pitched at 6.25 mm. A 0.05 mm thick guard ring grid was also incorporated on the anode side which can be used as a steering grid for better charge collection when biased appropriately. Full square back contact (cathode) was made on the opposite surface as shown in Figure 6.3 (d). In this work we have connected the guard ring grid to the ground in order to minimize the leakage current between the cathode and the anode pixels. Gold was used for all the metal contacts. The electrodes were formed by

RF/DC sputtering using semitransparent gold (Au) contact (150 – 250 Å). CZT crystals has a work function of 5.08 eV and are slightly p-type due to indium doping, while gold (Au) has a metal work function of 5.4 eV. With a p-type semiconductor, a metal with higher work function compared to that of the semiconductor ($\Phi_m > \Phi_s$) expected to form an Ohmic contact [72].

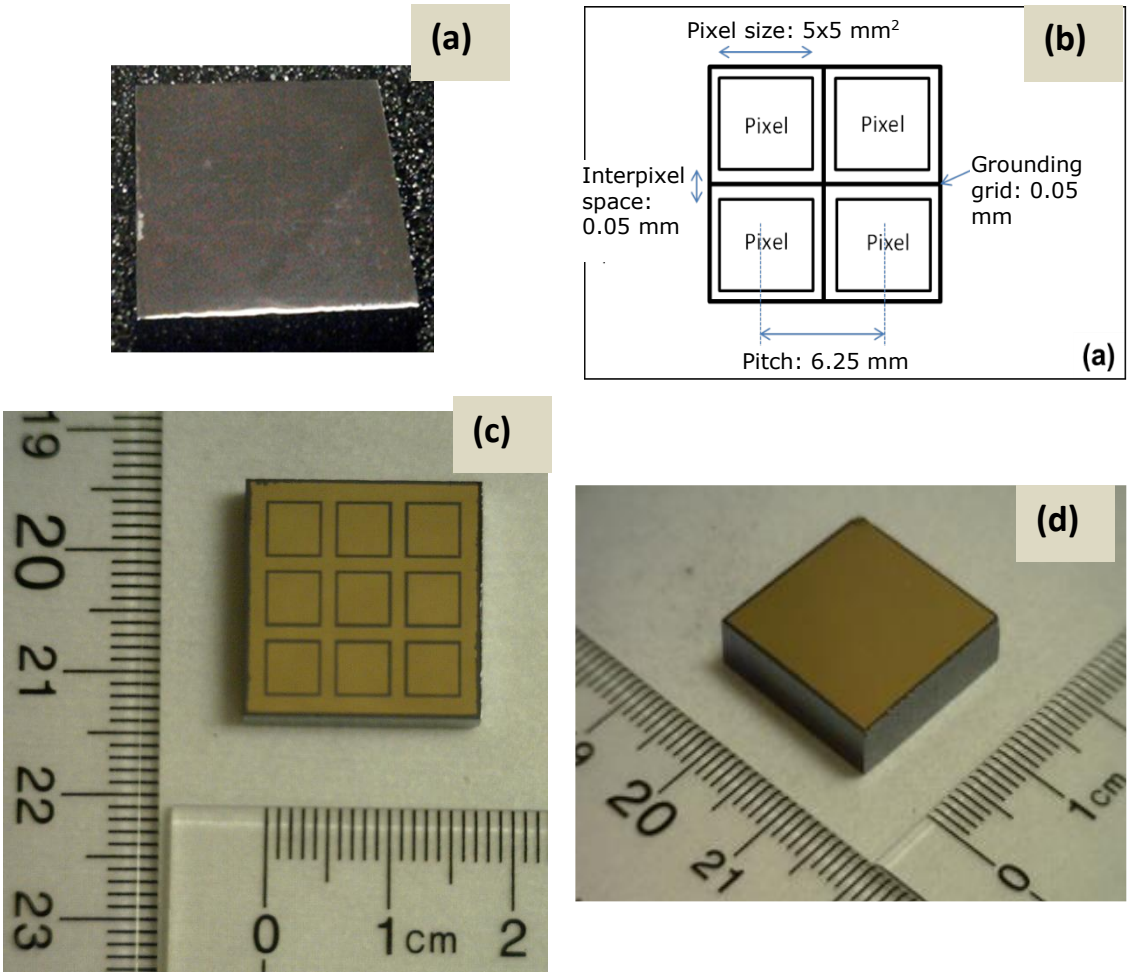

Figure 6.3 (a) A bare 20×20×5 mm^3 CZT crystal polished for detector fabrication; (b) Schematic of the pixelated detector showing four adjacent pixels and the various dimensions; (c) a photograph of the actual 3x3 pixelated CZT detector fabricated on polished crystal shown above; (d) full square back contact (cathode) fabricated on the back side of the same crystal.

6.5 Electrical Measurements

Current-voltage (I-V) measurements using metal-semiconductor junction was used to determine CZT crystal resistivity. A stable I-V characteristics and a high resistivity are required for high performance CZT detector as these will reduce the leakage current flowing through the detector under applied biased. I-V measurements were performed at room temperature (RT) under dark condition using a Keithley 237 High Voltage Source Measure Unit. I-V measurement was carried out by applying the bias on the Te rich face with the Cd rich face connected to ground. Figure 6.4 shows the current-voltage characteristic of the CZT detector. The detector showed a distinct asymmetry in the current behavior in the negative and positive bias regime indicating the presence of active deep centers at the surface which can render the Au/CZT interface as non-Ohmic. The leakage current at -1000V reverse bias was determined to be less than 5 nA. The electrical resistivity was estimated from inverse slope of the linear regression of current-voltage curve and using expression $\rho = R \cdot \frac{A}{L}$, where ρ = resistivity of the crystal in Ω-cm, R = resistance in Ω, A = contact area (cm^2), and L = thickness of the CZT crystal in cm. The electrical bulk resistivity was estimated to be ~ 10^{11} Ω-cm. This is high enough resistivity to fabricate a functional CZT radiation detector.

High frequency (100 kHz) Capacitance-voltage (C-V) measurements were carried out at room temperature (RT) under dark condition using a Keithley 590 CV Analyzer. C-V measurements were carried out to determine the full depletion bias. The capacitance at the metal-semiconductor junction of the Schottky device is a function of depletion width, and is described by the relationships given by:

$$C = \frac{\varepsilon \times \varepsilon_0 \times A}{W} \qquad 6.1$$

where C is capacitance, W is depletion width, A is the area of the junction, ε is the dielectric constant of semiconducotor material, and ε_0 is the permittivity in vacuum. The junction capacitance is inversely proportional to the applied bias as expressed in Equation 3.6. Figure 6.5 shows that under applied reverse bias, capacitance first decreases but then levels off, displaying that the detector is almost fully depleted, which is ideal for higher charge collection efficiency. The semi-insulating nature of the CZT crystal is confirmed by this C-V characteristic.

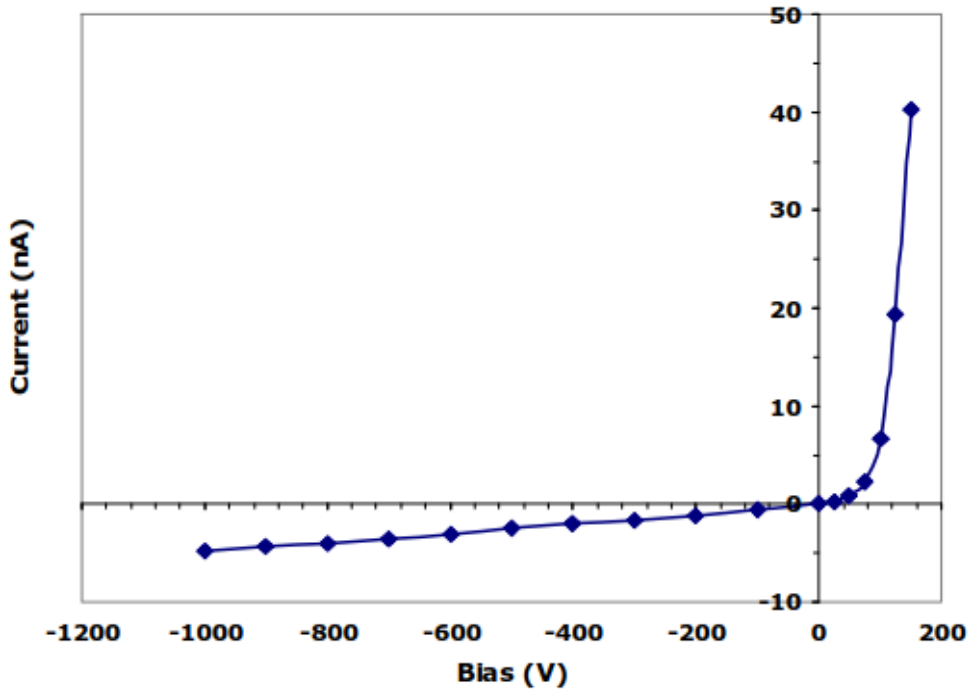

Figure 6.4. I-V characteristic of CZT detector at room temperature.

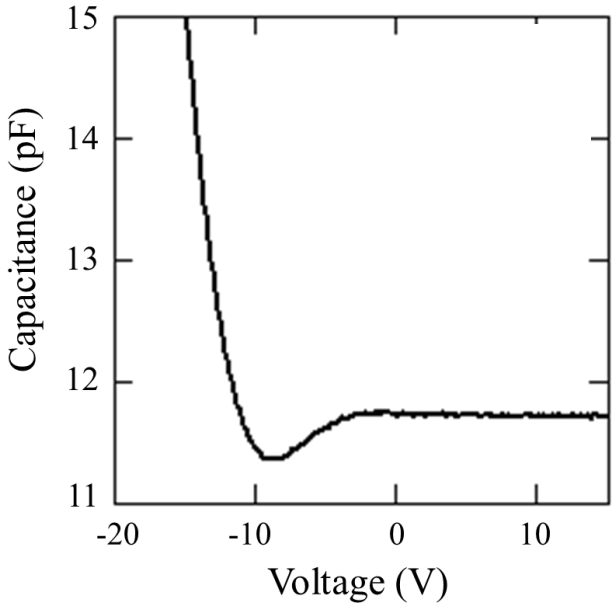

Figure 6.5. High frequency (100 kHz) capacitance-voltage (C-V) characteristic of the CZT detector

6.6 Charge Transport Measurements

The electron mobility-lifetime product ($\mu_e\tau_e$) is a common measurement used to characterize the charge transport properties of a detector, since it highlights both the electron trapping tendency and electron mobility, both of which are important to radiation detection. Based on the I-V characteristics, charge transport properties of electrons and holes were evaluated by measuring pulse positions at different biases. Upon reversal of the polarity of the applied bias, the mobility-lifetime product ($\mu\tau$) for electrons and holes were extracted using Hecht equation [103]:as expressed below.

$$CCE = \frac{Q_s}{Q_o} = \frac{\mu\tau_e V}{d^2}\left[1 - exp\left(\frac{-d^2}{\mu\tau_e V}\right)\right] \qquad 6.2$$

where Q_s is the total charge detected, Q_o is the expected total charge, V is the bias voltage, and d is the detector thickness. Hecht equation shows charge collection efficiency is also a function of the applied bias voltage. For mobility-lifetime product measurement, the detector was irradiated with a ^{241}Am alpha particle source on the cathode of the detector. After collecting the energy of the photopeaks versus bias voltage, the charge collection efficiency at each bias voltage is calculated by dividing the actual energy by the incident energy for ^{241}Am alpha particles (5.486 MeV). Then using charge collection efficiencies at an applied bias voltage, $\mu\tau_e$ values were obtained from Hecht equation. (Equation 6.2) as shown in Figure 6.6. After the curve fitting, the $\mu\tau_e$ of the planar CZT detector was determined to be 5.9×10^{-3} cm^2/V. Upon reversal of the polarity of the applied bias, the mobility-lifetime product for holes was determined in a similar way. Table 6.2 summarizes different electrical properties obtained for CZT detector.

Mobility of electron (μ_e) was calculated using a time-of-flight measurement [104] and employing the following relationship between drift velocity (v_d) acquired by an electron per unit applied electric field (E).

$$v_d = \mu_e E \tag{6.3}$$

Similar to mobility-lifetime measurement, time of flight measurement was conducted by irradiating cathode of the CZT detector with alpha particles from an ^{241}Am alpha source. Since electron-hole pairs are generated immediately at the cathode, the electrons will have to travel the entire distance of the detector to reach the anode. The electric field for each rise time is calculated using the relationship $E = \frac{V}{L}$, where V is the bias voltage and L is the detector thickness. From the slope of the linear fit of drift velocities

versus electric field plot, electron mobility of planar CZT detector was calculated to be 1192 cm^2/Vs.

Table 6.2. Electrical properties of CZT Detectors

Parameters	**CZT ($Cd_{0.9}Zn_{0.1}Te$)**
Bandgap [eV, 300 K]	1.56
Resistivity [Ω-cm]	~ 10^{11}
Leakage Current [nA]	≤5 (at -1000V)
Electron mobility [cm^2/V-s]	1192
Electron μτ product [cm^2/V]	6×10^{-3}
Hole μτ product [cm^2/V]	4.6×10^{-5}

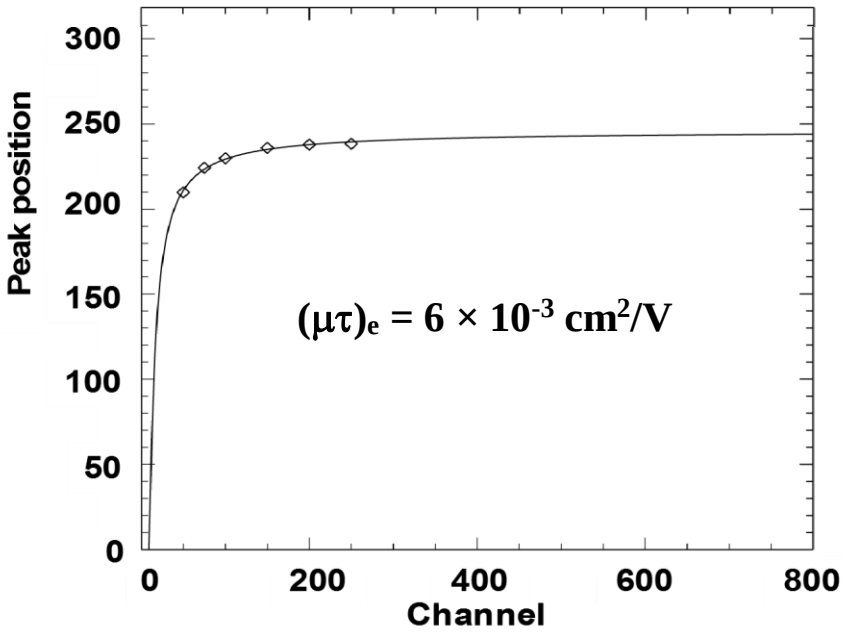

Figure 6.6. Peak position versus energy channel number used to obtain the value of mobility-lifetime product of electron ($\mu\tau_e$) by fitting Hecht equation.

6.7 CZT Detector Testing using Pulse Height Spectroscopy

The gamma spectroscopic measurements were carried out using an analog spectrometer comprising of a Cremat CR110 pre-amplifier, an Ortec 671 shaping amplifier and a Canberra Multiport II multichannel analyzer. The energy-resolutions of the detectors were measured in terms of full width at half maxima (FWHM) of the full energy peak obtained for gamma pulse-height spectra using a ^{137}Cs gamma source. An NI PCI-5122 digitizer card was used to digitize the charge pulses obtained from the detector-preamplifier assembly. A Labview based data-acquisition software was used to acquire and store the digitized pulses. PCI-5122 enables to acquire pulses with a sampling rate of 100 MS/s and 14 bit vertical resolution. A separate program was developed in our lab using Labview and MATLAB codes to process and analyze the digitized data. The data analyses involved digital semi-Gaussian shaping of the pulses followed by pulse-height determination. Figure 6.7 shows a schematic diagram of the detection system used for CZT detector.

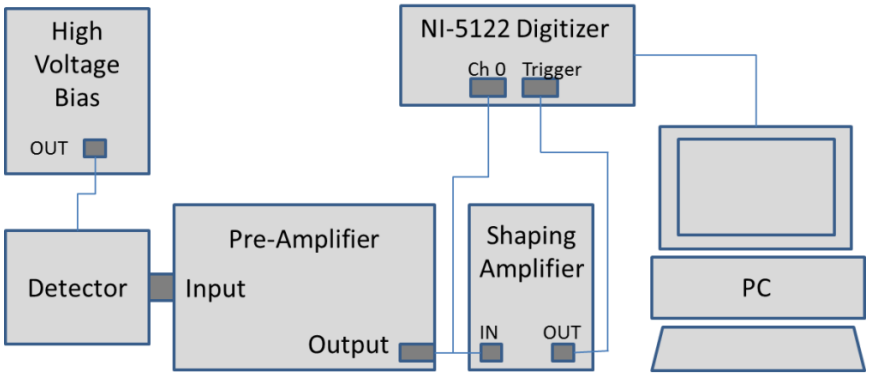

Figure 6.7. Schematic diagram of a digital nuclear detection measurement system at USC.

Figure 6.8 shows a ^{137}Cs pulse height spectrum (PHS) obtained using an arbitrarily chosen pixel with a bias of -1000 V applied to the cathode. The guard ring was connected to the ground during all the measurements. The 662 keV gamma peak was clearly resolved.

After performing Gaussian peak fitting, the FWHM of the gamma photopeak at 662 keV was calculated to be 1.51%. A ^{137}Cs (662 keV) PHS of a single-pixel CZT planar detector with guard ring fabricated from the same CZT ingot is shown in Figure 6.9 for comparison. The energy resolution for the 662 keV gamma peak was 2.6%. Comparing the two spectra it is evident that energy resolution has improved significantly with multi-pixel detector structure.

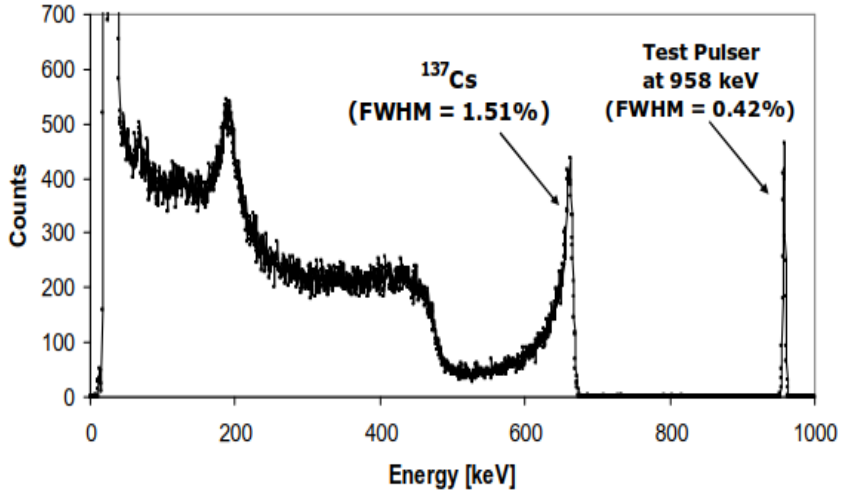

Figure 6.8 A ^{137}Cs Pulse height spectrum of a random pixel chosen from the 3x3 pixel CZT detector array.

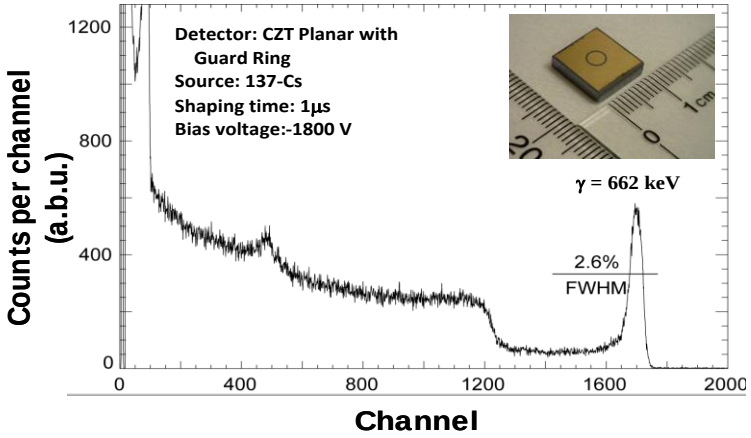

Figure 6.9. Pulse height spectrum obtained for CZT planar detector with guard ring using ^{137}Cs gamma radiation source. [105]

Figure 6.10 shows ^{137}Cs pulse height spectra for four adjacent pixels from the 3×3 CZT multi-pixel detector. All the spectra exhibited clearly resolved gamma peaks and similar spectral features. The spatial variation of energy resolution at 662 keV or variation in peak-to-valley (P-V) ratio from pixel to pixel PHS data under gamma radiation are yet to be investigated.

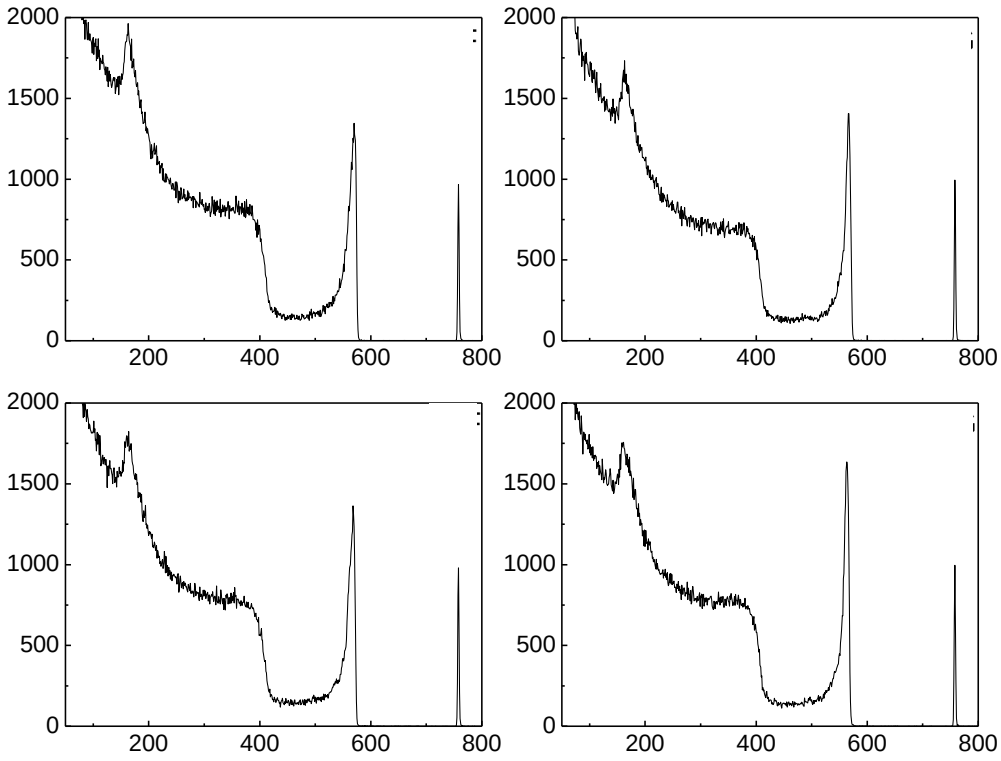

Figure 6.10. Pulse height spectrum obtained using a ^{137}Cs source from four adjacent pixels from a representative portion of the crystal.

6.8 CONCLUSION

$Cd_{0.9}Zn_{0.1}Te$ (CZT) based pixelated detector was fabricated and characterized for gamma ray detection. Large area CZT single crystals have been grown using a tellurium solvent method. A 3×3 guarded pixilated detector has been fabricated on a ~20×20×5 mm^3 crystal cut out from the grown ingot. A guard ring grid was used to reduce inter-pixel/inter-

electrode leakage. Current-voltage (I-V) measurements revealed a leakage current of ≤5 nA at an operating bias voltage of 1000 V and a resistivity of ~10^{11} Ω–cm. The mobility-lifetime product in this crystal was calculated to be 6×10^{-3} cm^2/V using alpha ray spectroscopic method. Using time of flight measurements, electron mobility was determined to be ~ 1192 $cm^2V^{-1}s^{-1}$. Gamma spectroscopy using a ^{137}Cs source on the pixelated structure showed fully resolved 662 keV gamma peaks for all the pixels, with percentage resolution (FWHM) as high as 1.51 %, which exhibited an improved resolution compared to single pixel CZT detector with guard ring.

CHAPTER 7

CONCLUSION, DISSEMINATION OF WORK, AND SUGGESTIONS FOR FUTURE WORK

7.1 CONCLUSION OF DISSERTATION WORK

In this dissertation two types of radiation detectors based on wide bandgap semiconductors were investigated: (i) Schottky barrier 4H-SiC detector for alpha particles and low energy x-ray radiation detection, and (ii) multi-pixelated CZT high-energy x-ray and gamma radiation detector. These detectors address the limitation of currently available detection systems in terms of detection efficiency, stability of response, speed of operation, and physical size due to requirement of cryogenic cooling. The SiC and CZT radiation detectors offer essential tools for monitoring and accounting of radioactive materials in nuclear power plants, nuclear waste management, national security, international nuclear nonproliferation treaty verification, nondestructive testing, medical imaging, and high energy astronomy. 4H-SiC devices exhibit extremely low leakage currents, high thermal conductivity, and high radiation hardness allowing detector operation well above room temperature and in high radiation background found in nuclear fuel processing environment in nuclear power plants and in upper atmosphere and outer space.

Schottky barrier alpha particle detectors were fabricated on 20 μm thick n-type 4H-SiC epitaxial layers. The epitaxial layers were grown by a hot wall chemical vapor deposition (CVD) process on n-type 4H-SiC (0001) substrates with 4^{o} off-cut towards the

[$11\bar{2}0$] direction. A micropipe density <1 cm^{-2} was observed for the SiC epilayer wafer. Schottky barriers were fabricated by depositing circular nickel contacts of ~10 mm^2 area. These epilayer 4H-SiC detectors exhibited high Schottky barrier height and an excellent current rectification with low leakage current of ~1 nA at a reverse bias of -170 V. Room temperature current-voltage measurements revealed Schottky barrier heights of >1.14 eV and ideality factor of ~1.19. Capacitance-Voltage measurements revealed a doping concentration of 2.9 x 10^{14} cm^{-3}.

Deep level transient spectroscopy (DLTS) was carried out to investigate defect levels and capture cross sections. From DLTS measurements, 5 defect levels (shallow and deep) were detected and identified as Ti(h) at E_c - (0.14 ± 0.01) eV, Ti(c) at E_c - (0.18 ± 0.01) eV, $Z_{1/2}$ at E_c - (0.62 ± 0.02) eV, EH_6 at E_c - (1.42 ± 0.04) eV, EH_7 at E_c - (1.52 ± 0.03) eV respectively. The origin of the Ti related defects are the substitutional impurities at hexagonal and cubic Si lattice sites, $Z_{1/2}$ defects are caused by interstitials and carbon vacancies, resolved levels of $EH_{6/7}$ (EH_6 and EH_7) are related to carbon vacancies and carbon-silicon di-vacancies.

A 0.1 μCi ^{241}Am radiation source was used to evaluate the detection performance of the fabricated detectors, and the alpha pulse height spectroscopy revealed a high energy resolution of ~0.38% FWHM energy resolution for 5.486 MeV alpha particles. Low microscopic and electrically active defect density and low effective doping concentration of 2.9 × 10^{14} cm^{-3} in the epilayers helped to achieve a high resolution even with a broad source. A diffusion length of ~13.6 μm for holes has been determined in these detectors following a calculation based on a drift-diffusion model. A noise analysis in terms of

equivalent noise charge revealed that the white series noise due to the detector capacitance has substantial effect on their spectroscopic performance.

An edge termination technique using passivating Si_3N_4 layer is developed and implemented on 4H-SiC radiation detectors. The effectiveness of edge termination was studied in terms of detector leakage current and alpha radiation detection performance. Results were compared with those of non-edge terminated detectors. Following edge termination with Si_3N_4, detectors exhibited a higher barrier height with improved rectifying characteristics and a leakage current of pA range, which was two orders of magnitude lower compared to detectors without edge termination. Alpha spectroscopy measurements conducted prior and subsequent to edge termination revealed a substantial improvement (~30%) in terms of energy resolution. The edge terminating layers collimated alpha particles incident on the detector window allowing more alpha particles to be deposited in the active region of the device. Furthermore, Schottky barrier detector with edge termination exhibited a significant improvement in electrical and defect characteristics, resulting in improved detector performance. DLTS results showed a reduction in the defect densities of $Z_{1/2}$ and no detectable presence of $EH_{6/7}$ defect levels in the Si_3N_4 edge terminated detector compared with a non-edge terminated detector from the same parent wafer. We suggest the C_i and Si_i atoms in participation induced stress/strain from lattice mismatch at the Si_3N_4/SiC interface layer may be responsible for the reduction of the $Z_{1/2}$, and $EH_{6/7}$ defect levels; however, further investigation is going on for correlation.

$Cd_{0.9}Zn_{0.1}Te$ (CZT) with high atomic number Z ~ 50, adequate gamma-ray energy absorption coefficient, low leakage currents at operating bias voltages, wide band gap at room temperature and high material density have become the most popular semiconductor

for compact high energy x- and gamma-ray detectors. Typical application of CZT detectors can be found in the field of homeland security, medical imaging, infrared focal plane array, environmental monitoring etc. In this study multi-pixelated CZT detector was fabricated and characterized for gamma ray detection. Small pixel geometry was selected for this current study to achieve unipolar (electron only) signal induction in order to circumvent limitation arise from the poor hole charge transport inherent in the CZT material.

A 3×3 guarded pixilated detector with guard ring has been fabricated on a ~20×20×5 mm^3 crystal cut out from the grown ingot. A guard ring grid was used to reduce inter-pixel/inter-electrode leakage. Current-voltage (I-V) measurements revealed a leakage current of ≤ 5 nA at an operating bias voltage of 1000 V and a resistivity of ~10^{11} Ω–cm. The mobility-lifetime product in this crystal was calculated to be 6 × 10^{-3} cm^2/V using alpha ray spectroscopic method. Using time of flight measurements, electron mobility was determined to be ~1192 $cm^2V^{-1}s^{-1}$. Gamma spectroscopy using a ^{137}Cs source on the pixelated structure showed fully resolved 662 keV gamma peaks for all the pixels, with percentage resolution (FWHM) as high as 1.51 %, which exhibited an improved resolution compared to single pixel CZT detector with guard ring.

7.2 Dissemination of Work

i. C. Oner, T. A. Chowdhury, E. Santi, and K. C. Mandal, "Deep Level Transient Spectroscopy and Pulse Height Measurements on High Resolution n-Type 4H-SiC Epitaxial Schottky Barrier Radiation Detectors," Invited Talk, Invited Paper, 2017 IEEE Nuclear Science Symposium & Medical Imaging Conference, and the 24rd International Symposium on Room-Temperature Semiconductor X-ray and

Gamma-ray Detectors, Oct. 21 –28, Atlanta, GA, *IEEE Conf. Record*, **R-11**, 5 pages, 2018.

ii. C. Oner, T. A. Chowdhury, and K. C. Mandal, "Crystal Growth and Characterization of $Cd_{0.9}Zn_{0.1}Te$ for Gamma-Ray Detectors: Thermally Stimulated Current (TSC), Electron Beam Induced Current (EBIC), and Pulse Height Spectroscopy (PHS)," 2017 IEEE Nuclear Science Symposium & Medical Imaging Conference, and the 24rd International Symposium on Room-Temperature Semiconductor X-ray and Gamma-ray Detectors, Oct. 21 – 28, Atlanta, GA, *IEEE Conf. Record*, **RO7-003**, 4 pages, 2018.

iii. C. Oner, J. W. Kleppinger, T. A. Chowdhury, M. Sajjad, E. Santi, and K. C. Mandal, "High Barrier Schottky Contacts on n-Type 4H-SiC Epitaxial Layers and High Performance Radiation Detectors," To be submitted: J. Appl. Physics, 2018.

iv. C. Oner, K. V. Nguyen, R. O. Pak, T. A. Chowdhury, and K. C. Mandal, "Investigation of Metal Contacts on High-Resistivity Large-Area Amorphous Selenium Alloy Films," 2015 IEEE Nuclear Science Symposium & Medical Imaging Conference, 22nd International Symposium on Room-Temperature Semiconductor X-ray and Gamma-ray Detectors, Oct. 31 – November 07, San Diego, CA, *IEEE Conf. Record*, **R3A-41**, 6 pages, 2016.

v. C. Oner, T. A. Chowdhury, R. O. Pak, and K. C. Mandal, "Improved radiation detectors on 4H-SiC epilayers by edge termination," Hard X-Ray, Gamma-Ray, and Neutron Detector Physics XVIII, *Proc. SPIE,* **9968**, 99680M-1-6, 2016.

vi. C. Oner, K. V. Nguyen, R. O. Pak, M. A. Mannan, and K. C. Mandal, "Investigation of thermally evaporated high resistive B-doped amorphous selenium alloy films

and metal contact studies," Hard X-Ray, Gamma-Ray, and Neutron Detector Physics XVII, *Proc. SPIE*, **9593**, 9593I-1-11, 2015.

vii. T. A. Chowdhury, C. Oner, and K.C. Mandal, "Synthesis and Characterization of Amorphous Selenium Alloys Radiation Detectors," 2017 IEEE Nuclear Science Symposium & Medical Imaging Conference, and the 24rd International Symposium on Room-Temperature Semiconductor X-ray and Gamma-ray Detectors, Oct. 21 – 28, Atlanta, GA, *IEEE Conf. Record*, **RO7-004**, 5 pages, 2017.

viii. K. C. Mandal, T. A. Chowdhury, C. Oner, and F. H. Ruddy, "Design and Response Testing of Boron-Diffused Silicon Carbide Neutron Detectors for Dosimetry and Monitoring Applications," Reactor Dosimetry: 16th International Symposium, *ASTM STP*, **1608**, 353-360, 2018.

ix. M. A. Mannan, K. V. Nguyen, R. O. Pak, C. Oner, and K. C. Mandal, "Deep Levels in n-type 4H-Silicon Carbide Epitaxial Layers Investigated by Deep-Level Transient Spectroscopy and Isochronal Annealing Studies," *IEEE Trans. Nucl. Sci.*, vol. **63**, no.2 pp. 1083-1090, 2016.

x. K. V. Nguyen, R. O. Pak, C. Oner, F. Zhao, and K. C. Mandal, "Investigation of 12 μm 4H-SiC epilayers for radiation detection and noise analysis of front-end readout electronics," 2015 IEEE Nuclear Science Symposium & Medical Imaging Conference 22nd International Symposium on Room-Temperature Semiconductor X-ray and Gamma-ray Detectors, Oct 31 – Nov 07, San Diego, CA, *IEEE Conf. Record*, **R5B-1**, 5 pages, 2016.

xi. R. O. Pak, K. V. Nguyen, C. Oner, T. A. Chowdhury, and K. C. Mandal, "Characterization of Cd0.9Zn0.1Te single crystals for radiation detectors," 2015

IEEE Nuclear Science Symposium & Medical Imaging Conference, 22nd International Symposium on Room-Temperature Semiconductor X-ray and Gamma-ray Detectors, Oct 31 – Nov 07, San Diego, CA, *IEEE Conf. Record*, **R5B-1**, 5 pages, 2016.

xii. M. A. Mannan, K. V. Nguyen, R. O. Pak, C. Oner and K. C. Mandal, "Surface passivation and isochronal annealing studies on n-type 4H-SiC epitaxial layer," Hard X-Ray, Gamma-Ray, and Neutron Detector Physics XVII, *Proc. SPIE*, **9593**, 95931H-1-11, 2015.

xiii. K. V. Nguyen, R. O. Pak, C. Oner, M. A. Mannan, and K. C. Mandal, "High-barrier Schottky contact on n-type 4H-SiC epitaxial layer and studies of defect levels by deep level transient spectroscopy (DLTS)," Hard X-Ray, Gamma-Ray, and Neutron Detector Physics XVII, *Proc. SPIE*, **9593**, 95930I-1-8, 2015.

xiv. R. O. Pak, K. V. Nguyen, C. Oner, M. A. Mannan, and K. C. Mandal, "Defect characterization of Cd0.9Zn0.1Te crystals using electron beam induced currrent (EBIC) imaging and thermally stimulated current (TSC) measurements," Hard X-Ray, Gamma-Ray, and Neutron Detector Physics XVII, *Proc. SPIE*, **9593**, 95931J-1-8, 2015.

7.3 Suggestions for Future Work

- Schottky barrier contact structures with nickel (Ni) have been fabricated on 20 µm thick 4H-SiC epitaxial layer. Different contact structures with varying work functions of the metals and higher thickness of the epitaxial layers could be studied to optimize detector performance with reduced leakage current and improved energy resolution.

- In 4H-SiC epitaxial layer, the electron mobility is significantly higher than hole mobility. To compensate poor hole transport properties, specialized detector structures such as multi-pixel with small pixel size, Frisch grid, co-planar, and drift detectors could be fabricated and performance evaluation could be compared to the planar detectors studied in this dissertation.
- Future efforts on 4H-SiC epilayer detectors could be carried out to lowering detector capacitance without reducing the active size of the detectors. In-detailed electronic noise analysis may reveal the possibility of achieving better performance with enhanced energy resolution by lowering the detector capacitance. This will reveal the white series noise due to the total input capacitance which may have substantial effects on detector performance.
- Improvement on 4H-SiC energy resolution and reduced leakage current is achieved by Si_3N_4 passivation in this work. SiO_2 and Si-O-N passivation could be studied to optimize detector performance further.
- For both 4H-SiC detector performance studies, defect delineating KOH etching may reveal the nature and type of various crystallographic defects and the results may be correlated to observe the impact of shallow and deep lying point and/or extended defects in the active region.
- Deep-level transient spectroscopy in the current mode (I-DLTS) could be applied to the CZT detectors for defect analysis. I-DLTS is an extremely sensitive technique for determining nature of defects present in the active region using current pulses. By using this technique, further information about the deep-lying defects can be

evaluated and quantified, which will assist in reducing shallow and deep defect levels in the grown CZT crystals.

- It has been studied two configurations for CZT gamma ray detectors, planar geometry and multiple small pixels. However, other types of detector geometries can be investigated such as co-planar, virtual Frisch grid, guard-ring, and drift detectors.

REFERENCES

[1] F. Nava, G. Bertuccio, A. Cavallini, and E. Vittone, "Silicon carbide and its use as a radiation detector material," *Meas. Sci. Technol.,* vol. **19**, pp. 102001-1-25, 2008.

[2] T. Hayashi, K. Asano, J. Suda, and T. Kimoto, "Enhancement and control of carrier lifetimes in p-type 4H-SiC epilayers," *J. Appl. Phys.,* vol. **112**, pp. 064503-1-6, 2012.

[3] F. H. Ruddy, J. G. Seidel, H. Chen, A. R. Dulloo, and S. Ryu, "High resolution alpha-particle spectrometry using 4H silicon carbide semiconductor detector," *IEEE Trans. Nucl. Sci.,* vol. **53**, pp. 1713-1718, 2006.

[4] Krishna C. Mandal, Sandeep K. Chaudhuri, Khai V. Nguyen, and Mohammad A. Mannan, "Correlation of Deep Levels with Detector Performance in 4H-SiC Epitaxial Schottky Barrier Alpha Detectors," *IEEE Trans. Nucl. Sci.,* vol. **61**, pp. 2338-2344, 2014.

[5] Khai V. Nguyen, Mohammad A. Mannan, and Krishna C. Mandal, "Improved n-Type 4H-SiC Epitaxial Radiation Detectors by Edge Termination," *IEEE Trans. Nucl. Sci.,* vol. **62**, pp. 3199-3206, 2015.

[6] Krishna C. Mandal, Ramesh M. Krishna, Peter G. Muzykov, Sandip. Das, and Tangali S. Sudarshan, "Characterization of Semi-Insulating 4H Silicon Carbide for Radiation Detectors," *IEEE Trans. Nucl. Sci.,* vol. **58**, pp. 1992-1999, 2011.

[7] Sandeep K. Chaudhuri, Kelvin. J. Zavalla, and Krishna C. Mandal, "Experimental determination of electron-hole pair creation energy in 4H-SiC epitaxial layer: An absolute calibration approach," *Appl. Phys. Lett.,* vol. **102**, pp. 031109-1-4, 2013.

[8] Krishna C. Mandal, Peter G. Muzykov, Ramesh M. Krishna, and J. Russell Terry, "Characterization of 4H-SiC Epitaxial Layers and High-Resistivity Bulk Crystals for Radiation Detectors," *IEEE Trans. Nucl. Sci.,* vol. **59**, pp. 1591-1596, 2012.

[9] Khai V. Nguyen and Krishna C. Mandal, "Ru-induced Deep Levels in Ru/4H-SiC Epilayer Schottky Diodes by Deep Level Transient Spectroscopy," *ECS J. Solid State Sci. Technol.,* vol. **5**, pp. P3078-P3081, 2016.

[10] Mohammad A. Mannan, Khai V. Nguyen, Rahmi O. Pak, Cihan Oner, and Krishna C. Mandal, "Deep Levels in n-Type 4H-Silicon Carbide Epitaxial

Layers Investigated by Deep Level Transient Spectroscopy and Isochronal Annealing Studies," *IEEE Trans. Nucl. Sci.,* vol. **63**, pp. 1083-1090, 2016.

[11] Krishna C. Mandal, Peter G. Muzykov, and J. Russell Terry, "Highly sensitive x-ray detectors in the low-energy range on n-type 4H-SiC epitaxial layers," *Appl. Phys. Lett.,* vol. **101**, pp. 051111-1-4, 2012.

[12] Peter G. Muzykov, Ramesh M. Krishna, and Krishna C. Mandal, "Temperature dependence of current conduction in semi-insulating 4H-SiC epitaxial layer," *Appl. Phys. Lett.,* vol. **100**, pp. 032101-1-4, 2012.

[13] T. E. Schlesinger, J. E. Toney, H. Yoon, E. Y. Lee, B. A. Brunett, L. Franks, and R. B. James, "Cadmium zinc telluride and its use as a nuclear radiation detector material," *Mater. Sci. Eng. R,* vol. **32**, pp. 103–189, 2001.

[14] Sandeep K. Chaudhuri, Kelvin J. Zavalla, Ramesh M. Krishna, and Krishna C. Mandal, "Biparametric analyses of charge trapping in $Cd_{0.9}Zn_{0.1}Te$ based virtual Frisch grid detectors," *J. Appl. Phys.,* vol. **113**, pp. 074504-1-6, 2013.

[15] Krishna C. Mandal, Ramesh M. Krishna, Peter G. Muzykov, and Tim C. Hayes, "Fabrication and characterization of high barrier $Cd_{0.9}Zn_{0.1}Te$ Schottky diodes for high resolution nuclear radiation detectors," *IEEE Trans. Nucl. Sci.,* vol. **59**, pp. 1504-1509, 2012.

[16] Rahmi O. Pak and Krishna C. Mandal, "Defect Levels in Nuclear Detector Grade $Cd_{0.9}Zn_{0.1}Te$ Crystals," *ECS J. Solid State Sci. Technol.,* vol. **5**, pp. P3037-P3040, 2016.

[17] Piyas Samanta and Krishna C. Mandal, "Leakage current conduction, hole injection and time-dependent dielectric breakdown of n-4H-SiC MOS capacitors during positive bias temperature stress," *J. Appl. Phys.,* vol. **121**, pp. 034501-1-13, 2017.

[18] Piyas Samanta and Krishna C. Mandal, "Simulation of temperature dependent dielectric breakdown in n^+-polySi/SiO_2/n-6H-SiC structures during Poole-Frenkel stress at positive gate bias," *J. Appl. Phys.,* vol. **120**, pp. 064505-1-10, 2016.

[19] P. G. Neudeck, D. J. Spry, L. Chen, N. F. Prokop, and M. J. Krasowski, "Demonstration of 4H-SiC Digital Integrated Circuits Above 800 °C," *IEEE Electron Device Lett.,* vol. **38**, pp. 1082-1085, 2017.

[20] Piyas Samanta and Krishna C. Mandal, "Hole injection and dielectric breakdown in 6H-SiC and 4H-SiC metal-oxide-semiconductor structures during substrate electron injection via Fowler-Nordheim tunneling," *Solid-State Electron.,* vol. **114**, pp. 60-68, 2015.

[21] P. G. Neudeck, "Electrical Impact of SiC Structural Crystal Defects on High Electric Field Devices," *Mater. Sci. Forum,* vols. **338-342**, pp. 1161-1166, 2000.

[22] Peter G. Muzykov, Ramesh M. Krishna, and Krishna C. Mandal, "Characterization of deep levels in n-type and semi-insulating 4H-SiC

epitaxial layers by thermally stimulated current spectroscopy," *J. Appl. Phys.*, vol. **111**, pp. 014910-1-7, 2012.

[23] P. G. Neudeck, R. S. Okojie, and L. -Y. Chen, "High-temperature electronics - a role for wide bandgap semiconductors? *Proc. IEEE,* vol. **90**, pp. 1065-1076, 2002.

[24] K. Shenai, "Future Prospects of Wide bandgap (WBG) Semiconductor Power Switching Devices," *IEEE Trans. Electron Devices,* vol. **62**, pp. 248-257, 2015.

[25] Krishna C. Mandal, Peter G. Muzykov, Ramesh M. Krishna, Tim C. Hayes, and T. S. Sudarshan, "Thermally stimulated current and high temperature resistivity measurements of 4H semi-insulating silicon carbide," *Solid State Commun.,* vol. **151**, pp. 532-535, 2011.

[26] R. Wang, I. B. Bhat, and T. P. Chow, "Epitaxial growth of n-type SiC using phosphine and nitrogen as the precursors," *J. Appl. Phys.,* vol. **92**, pp. 7587-7592, 2002.

[27] Peter G. Muzykov, Ramesh M. Krishna, Sandip Das, Tim C. Hayes, Tangali S. Sudarshan, and Krishna C. Mandal, "Characterization of 4H semi-insulating silicon carbide single crystals using electron beam induced current," *Mater. Lett.* vol. **65**, pp. 911-914, 2011.

[28] T. Kimoto and J. A. Cooper, "Fundamentals of Silicon Carbide Technology: Growth, Characterization, Defects and Applications," John Wiley, Singapore, 2014.

[29] F. Moscatelli, A. Scorzoni, A. Poggi, M. Bruzzi, S. Sciortino, S. Lagomarsino, G. Wagner, I. Mandic, R. Nipoti, "Radiation Hardness After Very High Neutron Irradiation of Minimum Ionizing Particle Detectors Based on 4H-SiC p^+n Junctions," *IEEE Trans. Nucl. Sci.,* vol. **53**, 1557-1563, 2006.

[30] S. Wang, M. Dudley, C. H. Carter, Jr., H. S. Kong, Proc. Mater. Res. Soc. Symp., vol. **339** ed H. Carter, G. Gildeblant, S. Nakamura and R. Nemanich (Pittsburgh, PA: Materials Research Society) (1994) 735 - 740.

[31] Q. Wahab, A. Ellison, C. Hallin, A. Henry, J. Di Persio, R. Martinez, E. Janzén, "Influence of Epitaxial Growth and Substrate Induced Defects on the Breakdown of High-voltage 4H-SiC Schottky Diodes," *Mater. Sci. Forum,* vols. **338-342**, 1175-1178, 2000.

[32] R. V. Badcock and H. C. Chang, "SiC Neutron Detectors for High Temperature Operation, Neutron Dosimetry," *Proceedings of the Symposium on Neutron Detection, Dosimetry and Standardization,* vol. **1**, pp. 613-622, 1962.

[33] F. Nava, P. Vanni, C. Lanzieri and C. Canali, "Epitaxial silicon carbide charge particle detectors," *Nucl. Instrum. Methods Phys. Res. A,* vol. **437**, pp. 354-358, 1999.

[34] H. Ruddy, A. R. Dulloo, J. G. Seidel, S. Seshari and L. B. Rowland, "Development of a Silicon Carbide Radiation Detector," *IEEE Trans. Nucl. Sci.*, vol. **45**, pp. 536-541, 1998.

[35] F. Ruddy, J. Seidel and P. Sellin, "High-resolution alpha spectrometry with a thin-window silicon carbide semiconductor detector," *Proceedings of the IEEE Nuclear Science Symposium Conference Record* (NSS/MIC), pp. 2201-2206, 2009.

[36] F. H. Ruddy, J. G. Seidel, H. Chen, A. R. Dulloo, and S. Ryu,"High resolution alpha-particle spectrometry using 4H silicon carbide semiconductor detector," *IEEE Trans. Nucl. Sci*., vol. **53**, pp. 1713-1718, 2006.

[37] K. Danno and T. Kimoto, "Deep level transient spectroscopy on as-grown and electron–irradiated p-type 4H-SiC epilayers," *J. Appl. Phys*., vol. **101**, pp. 103704-1-5, 2007.

[38] Krishna C. Mandal, Peter G. Muzykov, Sandeep K. Chaudhuri, and J. Russell Terry, "Low energy x-ray and γ-ray detectors fabricated on n-type 4H-SiC epitaxial layer," *IEEE Trans. Nucl. Sci.,* vol. **60**, pp. 2888-2893, 2013.

[39] Sandeep K. Chaudhuri, Ramesh M. Krishna, Kelvin J. Zavalla, and Krishna C. Mandal, "Schottky barrier detectors on 4H-SiC n-type epitaxial layer for alpha particles," *Nucl. Instrum. Methods Phys. Res. A*, vol. **701**, pp. 214-220, 2013.

[40] I. Pintilie, L. Pintilie, K. Irmscher, and B. Thomas, "Deep Levels in As-Grown 4H-SiC Epitaxial Layers and their Correlation with CVD Parameters," *Mater. Sci. Forum,* vols. **433–436**, pp. 463–466, 2003.

[41] C. G. Hemmingsson, N. T. Son, O. Kordina, E. Janzén, J. L. Lindström, S. Savage, and N. Nordell, "Deep level defects in electron-irradiated 4H SiC epitaxial layers," *J. Appl. Phys.,* vol. **81**, pp. 6155-6159, 1997.

[42] Sandeep K. Chaudhuri, Kelvin J. Zavalla, and Krishna C. Mandal, "High Resolution Alpha Particle Detection Using 4H-SiC Epitaxial Layers: Fabrication, Characterization, and Noise Analysis," *Nucl. Instrum. Methods Phys. Res. A*, vol. **728**, pp. 97-101, 2013.

[43] P. A. Luke, and M. Amman, "Room-Temperature Replacement for Ge Detectors-Are We There Yet?," *IEEE Trans. Nucl. Sci.,* vol. **54**, no. 4, pp. 834-842, 2007.

[44] K. C. Mandal, R. O. Pak, C. Oner, and T. A. Chowdhury, "High Temperature Measurements of N-Type 4H-SiC Epitaxial Schottky Barrier Radiation Detectors," Paper No. 2663, Invited Talk, IEEE MIC-NSS-RTSD, Strasbourg, Oct. 29 – Nov. 06, 2016.

[45] G. Bertuccio, D. Puglisi, A. Pullia, and C. Lanzieri, "X-γ Ray Spectroscopy With Semi-Insulating 4H-Silicon Carbide," vol. **60**, 1436-1441, 2013.

[46] G. Lioliou, H. K. Chan, T. Gohil, K. V. Sassilevski, N. G. Wright, A. B. Horsfall, A. M. Barnett, "4H-SiC Schottky diode arrays for X-ray detection," *Nucl. Instrum. Methods Phys. Res. A*, vol. **840**, 145-152, 2016.

[47] F. H. Ruddy and J. G. Seidel, “The Effects of Intense Gamma Irradiation on the Alpha-Particle Response of SiC Radiation Detectors,” *Nucl. Instrum. Methods Phys. Res. B,* vol. **263**, 163-168, 2007.

[48] G. F. Knoll, Radiation Detection and Measurement, 3rd ed., New York: John Wiley & Sons, Inc., 2000.

[49] P. N. Luke, R. H. Pehl, and F. A. Dilmanian, “A 140-element Ge detector fabricated with amorphous Ge blocking contacts,” *IEEE Trans. Nucl. Sci.,* vol. **41**, pp. 976-978, 1994.

[50] S. D. Sordo, L. Abbene, E. Caroli, A. M. Mancini, A. Zappetteni, and P. Ubertini, "Progress in the Development of CdTe and CdZnTe Semiconductor Radiation Detectors for Astrophysical and Medical Applications," *Sensors,* vol. **9**, pp. 3491-3526, 2009.

[51] Ramesh M. Krishna, Peter G. Muzykov, and Krishna C. Mandal, “Electron beam induced current imaging of dislocations in $Cd_{0.9}Zn_{0.1}Te$ crystal,” *Journal of Physics and Chemistry of Solids,* vol. **74**, pp. 170-173, 2013.

[52] K. C. Mandal, S. H. Kang, M. Choi, A. Kargar, M. J. Harrison, D. S. McGregor, A. E. Bolotnikov, G. A. Carini, G. C. Camarda, and R. B. James, “Characterization of Low-Defect $Cd_{0.9}Zn_{0.1}Te$ Crystals for High-Performance Frisch Collar Detectors,” *IEEE Trans. Nucl. Sci.,* vol. **54**, pp. 802-806, 2007.

[53] K. C. Mandal, S. H. Kang, M. Choi, J. Bello, L. Zheng, H. Zhang, M. Groza, U. N. Roy, A. Burger, G. E. Jellison, D. E. Holcomb, G. W. Wright, J. A. Williams, “Simulation, modeling, and crystal growth of $Cd_{0.9}Zn_{0.1}Te$ for nuclear spectrometers,” *J. Electron. Mater.* vol. **35**, pp. 1251-1256, 2006.

[54] U. N. Roy, A. Gueorguiev, S. Weiler, and J. Stein, “Growth of spectroscopic grade $Cd_{0.9}Zn_{0.1}Te$:In by THM technique,” *J. Crystal Growth,* vol. **312**, pp. 33-36, 2009.

[55] R. M. Krishna, S. K. Chaudhuri, K. J. Zavalla, and K. C. Mandal, "Characterization of $Cd_{0.9}Zn_{0.1}Te$ based virtual Frisch grid detectors for high energy gamma ray detection," *Nucl. Instrum. Methods in Phys. Res. A,* vol. **701**, pp. 208-213, 2013.

[56] B. Milbrath, A. Peurrung, M. Bliss, and W. Weber, "Radiation detector materials: An overview," *J. Materials Research,* vol. **23**, pp. 2561-2581, 2008.

[57] T. E. Schlesinger and R. B. James, Eds., Semiconductors for Room Temperature Nuclear Detector Applications, San Diego: Academic Press Inc., 1995.

[58] A. E. Bolotnikov, K. Ackley, G. S. Camarda, C. Chercher, Y. Cui, G. De Geronimo, J. Fried, D. Hodges, A. Hossain, W. Lee, G. Mahler, M. Maritato, M. Petryk, U. Roy, C. Salwen, E. Vernon, G. Yang, and R. B. James, “An array of virtual Frisch-grid CdZnTe detectors and a front-end application-specific integrated circuit for large-area position-sensitive gamma-ray cameras,” *Rev. Sci. Instrum.,* vol. **86**, pp. 073114-1-5, 2015.

[59] L. S. Ramsdell, "Studies on silicon carbide," *American Mineralogist,* vol. **32**, pp. 64-82, 1947.

[60] T. Kinoshita, K. M. Itoh, J. Muto, M. Schadt, G. Pensl, and K. Takeda, "Calculation of the Anisotropy of the Hall Mobility in n-type 4H- and 6H-SiC," *Materials Sci. Forum,* vols. **264–268**, pp. 295-298, 1998.

[61] W. J. Choyke, H. Matsunami, and G. Pensi, Silicon Carbide: A Review of Fundamental Questions and Applications to Current Device Technology, Berlin: Wiley-VCH, 1997.

[62] G. L. Harris, "Properties of SiC," London: INSPEC, 1995.

[63] D. J. Spry, P. G. Neudeck, L. Chen, C. W. Chang, D. Lukco, G. M. Beheim, "4H-SiC JFET multilayer integrated circuit technologies tested up to 1000 K," *ECS Trans*., vol. **69**, pp. 113-121, 2015.

[64] B. Ellis and T. S. Moss, "The conduction bands in 6H and 15R silicon carbide, Hall effect and infrared Faraday rotation measurements," *Proc. Royal Soc. London,* London, 1967.

[65] G. A. Lomakina, "Silicon carbide Proceeding," in *3rd International Conference on Silicon Carbide,* Miami, 1973.

[66] S. Karmann, W. Suttrop, A. Schoner, M. Schadt, C. Haberstroh, F. Engeibrecht, R. Helbig, G. Penal, R. A. Stein, and S. Leibenzeder, "Chemical vapor deposition and characterization of undoped and nitrogen-doped single crystalline 6H-SiC," *J. Appl. Phys.*, vol. **72**, pp. 5437-5442, 1992.

[67] Y. M. Tairov and V. F. Tsvetkov, "General principles of growing large-size single crystals of various silicon carbide polytypes," *J. Crystal Growth,* vol. **52**, pp. 146-150, 1981.

[68] S. G. Muller, R. C. Glass, H. M. Hobgood, V. F. Tsvetkov, M. Brady, D. Henshall, J. R. Jenny, D. Malta, and C. H. Carter, "The status of SiC bulk growth from an industrial point of view," *J. Crystal Growth,* vol. **211**, pp. 325-332, 2000.

[69] J. J. Sumakeris, J. R. Jenny, and A. R. Powell, "Bulk crystal growth, epitaxy, and defect reduction in silicon carbide materials for microwave and power devices," *MRS Bulletin,* vol. **30**, pp. 280-286, 2005.

[70] A. R. Powell and L. B. Rowland, "SiC materials - Progress, status, and potential roadblocks," *Proceedings of the IEEE,* vol. **90**, pp. 942-955, 2002.

[71] M. B. H. Breese, "A theory of ion beam induced charge collection," *J. Appl. Phys.*, vol. **74**, pp. 3789-3799, 1993.

[72] E. H. Rhoderick and R. H. Williams, *Metal-Semiconductor Contacts*. Oxford: Clarendon, 1998.

[73] S. M. Sze and K. K. Ng, "Metal-Semiconductor Contacts," in *Physics of Semiconductor devices,* Hoboken, New Jersey, John Wiley & Sons, Inc., 2007, pp. 134-190.

[74] A. Itoh and H. Matsunami, “Analysis of Schottky Barrier Heights of Metal/SiC Contacts and its Possible Application to High-Voltage Rectifying Devices,” *phys. status solidi (a),* vol. **162**, pp. 389-408, 1997.

[75] W. Schottky, “On the semiconductor theory of blocking and point contact rectifiers,” *Z. Phys.,* vol. **118**, pp. 539–592, 1942.

[76] R. T. Tung, "Electron transport at metal-semiconductor interfaces: General theory," *Physical Review B,* vol. **45**, pp. 13509-13523, 1992.

[77] J. Zhang, L. Storasta, J. P. Bergman, N. T. Son, and E. Janzen, “Electrically active defects in n-type 4H–silicon carbide grown in a vertical hot-wall reactor,” *J. Appl. Phys.,* vol. **93**, pp. 4708-4714, 2003.

[78] T. Dalibor and G. Pensl, “Electrical properties of the titanium acceptor in silicon carbide,” *Phys. Rev. B,* vol. **55**, pp. 13618-13624, 1997.

[79] G. Bertuccio and A. Pullia, “A method for the determination of the noise parameters in preamplifying systems for semiconductor radiation detectors,” *Rev. Sci. Instrum.,* vol. **64**, pp. 3294-3298, 1993.

[80] K. V. Nguyen, R. O. Pak, C. Oner, M. A. Mannan, and K. C. Mandal, “High-barrier Schottky contact on n-type 4H-SiC epitaxial layer and studies of defect levels by deep level transient spectroscopy (DLTS),” *SPIE Proc.*, vol. **9593**, pp. 95930I-1-8, 2015.

[81] R. Waters and B. V. Zeghbroeck, “Temperature-dependent tunneling through thermally grown SiO_2 on n-type 4H- and 6H-SiC,” *Appl. Phys. Lett.*, vol. **76**, pp. 1039-1041, 2000.

[82] P. Samanta and K. C. Mandal "Leakage Current Conduction and Reliability Assessment of Passivating Thin Silicon Dioxide Films on n-4H-SiC," *SPIE Proc.,* vol. **9968**, pp. 99680E-1-12, 2016.

[83] L. Gelczuk, M. Dabrowska-Szata, M. Sochacki, and J. Szmidt, “Characterization of deep electron traps in 4H-SiC Junction Barrier Schottky rectifiers,” *Solid-State Electron.,* vol. **94**, pp. 56-60, 2014.

[84] A. Castaldini, A. Cavallini, L. Polenta, F. Nava, C. Canali, and C.Lanzieri, “Deep levels in silicon carbide Schottky diodes,” *Appl. Surf. Sci.,* vol. **187,** pp. 248-252, 2002.

[85] L. Storasta, J. P. Bergman, E. Janzen, A. Henry, and J. Lu, “Deep levels created by low energy electron irradiation in 4H-SiC,” *J. Appl. Phys.,* vol. **96**, pp. 4909-4916, 2004.

[86] N. Iwamoto, B. C. Johnson, N. Hoshino, M. Ito, H. Tsuchida, K. Kojima, and T. Ohshima, “Defect-induced performance degradation of 4H-SiC Schottky barrier diode particle detectors,” *J. Appl. Phys.,* vol. **113**, pp. 143714-1-5, 2013.

[87] C. G. Hemmingson, N. T. Son, O. Kordina, J. P. Bergman, E. Janzen, J. L. Lindstrom, S. Savage, and N. Nordell, “Deep level defects in electron-

irradiated 4H-SiC epitaxial layers," *J. Appl. Phys.*, vol. **81**, pp. 6155-6159, 1997.

[88] T. A. G. Eberlein, C. J. Fall, R. Jones, P. R. Briddon, and S. Öberg, "Alphabet luminescence lines in 4H−SiC," *Phys. Rev. B*, vol. **65**, pp. 184108-1-4, 2002.

[89] T. Kimoto, K. Danno, and J. Suda, "Lifetime-killing defects in 4H-SiC epilayers and lifetime control by low-energy electron irradiation," *phys. status solidi B*, vol. **245**, pp. 1327-1336, 2008.

[90] K. Danno and T. Kimoto, "Investigation of deep levels in n-type 4H-SiC epilayers irradiated with low-energy electrons," *J. Appl. Phys.*, vol. **100**, pp. 113728-1-6, 2006.

[91] J. Wong-Leung and B. G. Svensson, "Electric field assisted annealing and formation of prominent deep-level defect in ion-implanted n-type 4H-SiC," *Appl. Phys. Lett.*, vol. **92**, pp. 142105-1-3, 2008.

[92] S. A. Reshanov, G. Pensl, K. Danno, T. Kimoto, S. Hishiki, T. Ohshima, H. Itoh, F. Yan, R. P. Devaty, and W. J. Choyke, "Effect of the Schottky barrier height on the detection of midgap levels in 4H-SiC by deep level transient spectroscopy," *J. Appl. Phys.*, vol. **102**, pp. 113702-1-5, 2007.

[93] M. A. Mannan, S. K. Chaudhuri, K. V. Nguyen, and K. C. Mandal, "Effect of $Z_{1/2}$, EH_5 and Ci1 deep defects on the perormance of n-type 4H-SiC epitaxial layers Schottky detectors: Alpha spectroscopy and deep level transient spectroscopy studies," *J. Appl. Phys., vol.* **115**, pp. 224504-1-6, 2014.

[94] G. Alfieri and T. Kimoto, "Capacitance spectroscopy study of deep levels in Cl-implanted 4H-SiC," *J. Appl. Phys.*, vol. **112**, pp. 63717-1-4, 2012.

[95] T. Hiyoshi and T. Kimoto, "Reduction of deep levels and improvement of carrier lifetime in n-type 4H-SiC by thermal oxidation," *Appl. Phys. Express*, vol. **2**, pp. 041101-1-3, 2009.

[96] K. Kawahara, J. Suda, and T. Kimoto, "Deep levels generated by thermal oxidation in n-type 4H-SiC," *Appl. Phys. Express*, vol. **6**, pp. 051301-1-4, 2013.

[97] H. H. Barrett, J. D. Eskin, and H. B. Barber, "Charge Transport in Arrays of Semiconductor Gamma-Ray Detectors," *Phys. Rev. Lett.*, vol. **75**, pp. 156-159, 1995.

[98] D. S. McGregor, Z. He, H. A. Seifert, D. K. Wehe, and R. A. Rojeski, "Single charge carrier type sensing with a parallel strip pseudo-Frisch-grid CdZnTe semiconductor radiation detector," *Appl. Phys. Lett.*, vol. **72**, pp. 792-794, 1998.

[99] P. N. Luke, "Single-polarity charge sensing in ionization detectors using coplanar electrodes," *Appl. Phys. Lett.*, vol. **65**, pp. 2884-2886, 1994.

[100] J. L. Matteson, W. Coburn, F. Duttaweiler, T. M. Gasaway, W. A. Heindl. P.C. Leblanc, D. MacDonald, M. R. Pelling, L. Peterson, R. Rothschild, R. T.

Skelton, P. I. Hink, and C. Crabtree, “CdZnTe strip detectors for high energy x-ray astronomy,” *Proc. SPIE*, vol. **2859**, pp. 58-73, 1996.

[101] G. A. Carini, A. E. Bolotnikov, G. S. Camarda, G. W. Wright, R. B. James, and L. Li, “Effect of Te precipitates on the performance of CdZnTe detectors,” *Appl. Phys. Lett.*, vol. **88**, pp. 143515-143517, 2006.

[102] A. E. Bolotnikov, G. S. Camarda, G. A. Carini, Y. Cui, L. Li, and R. B. James, “Cumulative effects of Te precipitates in CdZnTe radiation detectors,” *Nucl. Instrum. Methods in Phys. Res. A*, vol. **571**, pp. 687-698, 2007.

[103] K. Hecht, "Zum Mechanismus des lichtelektrischen prim arstroms in isolierenden Kristallen," *Z. Physik*, vol. **77**, pp. 235-245, 1932.

[104] J. C. Erickson, H. W. Yao, R. B. James, H. Hermon, and M. Greaves, "Time of Flight Experimental Studies of CdZnTe Radiation Detectors," *J. Electronic Materials*, vol. **29**, pp. 699-703, 2000.

[105] Rahmi O. Pak, Ph.D. Dissertation, Titled: “Investigation of Wide Bandgap Semiconductor Devices for Radiation Detection Applications,” Electrical Engineering Department, University of South Carolina, Columbia, USA, 2016.